The ATLAS[3D] project - XII. Recovery of the mass-to-light ratio of simulated early-type barred galaxies with axisymmetric dynamical models.

Pierre-Yves Lablanche[1,2]⋆, Michele Cappellari[3], Eric Emsellem[2,1],
Frédéric Bournaud[4], Leo Michel-Dansac[1], Katherine Alatalo[6], Leo Blitz[6], Maxime Bois[7],
Martin Bureau[3], Roger L. Davies[3], Timothy A. Davis[3], P. T. de Zeeuw[2,8], Pierre-Alain Duc[4],
Sadegh Khochfar[9], Davor Krajnović[2], Harald Kuntschner[2], Raffaella Morganti[10,11],
Richard M. McDermid [12], Thorsten Naab[13], Tom Oosterloo[10,11], Marc Sarzi[14], Nicholas Scott[3],
Paolo Serra[10], Anne-Marie Weijmans[15]† and Lisa M. Young[5]

[1]*Université Lyon 1, Observatoire de Lyon, Centre de Recherche Astrophysique de Lyon*
and Ecole Normale Supérieure de Lyon, 9 avenue Charles André, F-69230 Saint-Genis Laval, France
[2]*European Southern Observatory, Karl-Schwarzschild-Str. 2, 85748 Garching, Germany*
[3]*Sub-department of Astrophysics, Department of Physics, University of Oxford, Denys Wilkinson Building, Keble Road, Oxford OX1 3RH*
[4]*Laboratoire AIM Paris-Saclay, CEA/IRFU/SAp CNRS Université Paris Diderot, 91191 Gif-sur-Yvette Cedex, France*
[5]*Physics Department, New Mexico Institute of Mining and Technology, Socorro, NM 87801, USA*
[6]*Department of Astronomy, Campbell Hall, University of California, Berkeley, CA 94720, USA*
[7]*Observatoire de Paris, LERMA and CNRS, 61 Av. de l'Observatoire, F-75014 Paris, France*
[8]*Sterrewacht Leiden, Leiden University, Postbus 9513, 2300 RA Leiden, the Netherlands*
[9]*Max Planck Institut für extraterrestrische Physik, PO Box 1312, D-85478 Garching, Germany*
[10]*Netherlands Institute for Radio Astronomy (ASTRON), Postbus 2, 7990 AA Dwingeloo, The Netherlands*
[11]*Kapteyn Astronomical Institute, University of Groningen, Postbus 800, 9700 AV Groningen, The Netherlands*
[12]*Gemini Observatory, Northern Operations Centre, 670 N. A'ohoku Place, Hilo, HI 96720, USA*
[13]*Max-Planck-Institut für Astrophysik, Karl-Schwarzschild-Str. 1, 85741 Garching, Germany*
[14]*Centre for Astrophysics Research, University of Hertfordshire, Hatfield, Herts AL1 9AB, UK*
[15]*Dunlap Institute for Astronomy & Astrophysics, University of Toronto, 50 St. George Street, Toronto, ON M5S 3H4, Canada*

ABSTRACT

We investigate the accuracy in the recovery of the stellar dynamics of barred galaxies when using axisymmetric dynamical models. We do this by trying to recover the mass-to-light ratio (M/L) and the anisotropy of realistic galaxy simulations using the Jeans Anisotropic Multi-Gaussian Expansion (JAM) method. However, given that the biases we find are mostly due to **an application of an axisymmetric modeling algorithm to a non-axisymmetric system and in particular to** inaccuracies in the de-projected mass model, our results are relevant for general axisymmetric modelling methods. We run N-body collisionless simulations to build a library with various luminosity distribution, constructed to mimic real individual galaxies, with realistic anisotropy. The final result of our evolved library of simulations contains both barred and unbarred galaxies. The JAM method assumes an axisymmetric mass distribution, and we adopt a spatially constant M/L and anisotropy $\beta_z = 1 - \sigma_z^2/\sigma_R^2$ distributions. The models are fitted to two-dimensional maps of the second velocity moments $V_{\rm rms} = \sqrt{V^2 + \sigma^2}$ of the simulations for various viewing angles (position angle of the bar and inclination of the galaxy). We find that the inclination is generally well recovered by the JAM models, for both barred and unbarred simulations. For unbarred simulations the M/L is also accurately recovered, with negligible median bias and with a maximum one of just $\Delta(M/L) < 1.5\%$ when the galaxy is not too close to face on. At very low inclinations ($i \lesssim 30°$) the M/L can be significantly overestimated (9% in our tests, but errors can be larger for very face-on views). This is in agreement with previous studies. For barred simulations the M/L is on average (when PA$= 45°$) essentially unbiased, but we measure an over/under estimation of up to $\Delta(M/L) = 15\%$ in our tests. The sign of the M/L bias depends on the position angle of the bar as expected: overestimation occurs when the bar is closer to end-on, due to the increased stellar motion along the line-of-sight, and underestimation otherwise. For unbarred simulations, the JAM models are able to recover the mean value of the anisotropy with bias $\Delta\beta_z \lesssim 0.1$, within the region constrained by the kinematics. However when a bar is present, or for nearly face-on models, the recovered anisotropy varies wildly, with biases up to $\Delta\beta_z \approx 0.3$.

Key words: methods: N-body simulations – galaxies: kinematics and dynamics – galaxies: elliptical and lenticular, cD – galaxies: structure

1 INTRODUCTION

The determination of the masses (or equivalently mass-to-light ratios) of gas-poor galaxies has been an important issue since the discovery that galaxies are stellar systems like the Milky Way, with mass being a strong driver of many of their properties. Dynamical modelling methods of increased sophistication have been developed over the past decades, all based on the assumption that galaxies can be described as stationary systems. The first attempt at measuring dynamical masses of galaxies were based on the spherical virial equations (Poveda 1958; Spitzer 1969). These methods have the disadvantage that, for accurate results, they need to assume self-similarity in the galaxy light and mass distribution. More accurate methods allow for axisymmetry and take the galaxy light distribution into account. The first detailed axisymmetric models of real galaxies were based on the Jeans (1922) equations and assumed a distribution function that depends on two (out of three) integrals of motion (e.g Binney et al. 1990; van der Marel et al. 1990; Emsellem et al. 1994b), but special classes of three-integral models were also used. Axisymmetric methods were developed to allow for a general orbital distribution, based on Schwarzschild (1979) numerical orbital superposition method (e.g. Cretton et al. 1999; van der Marel et al. 1998; Gebhardt et al. 2003; Thomas et al. 2004; Cappellari et al. 2006). Currently the most general available models assume

galaxies can be approximated by a stationary triaxial shape (e.g. de Lorenzi et al. 2007; van den Bosch et al. 2008).

The above modelling techniques were developed under the assumption that gas-poor galaxies can be well described by stationary axisymmetric or triaxial spheroidal systems. However a key initial result of the ATLAS[3D] survey (Cappellari et al. 2011a, hereafter Paper I) is the fact that nearby gas-poor galaxies are actually dominated (86 per cent of them) by fast rotators (Krajnović et al. 2011; Emsellem et al. 2011, hereafter Paper II and Paper III), often with significant disk components and resembling spiral galaxies with the dust removed (Cappellari et al. 2011b), 30% of which at least are barred. The presence of these bars is a difficult problem for all modelling methods and therefore motivates the present study.

Bars are density waves which results in a tumbling potential: this figure rotation is often ignored in the popular dynamical modelling methods described above. Dynamical models of barred galaxies have been constructed in the past (e.g. Pfenniger 1984; Häfner et al. 2000; Zhao 1996). However, the existence of intrinsic degeneracies in the dynamical modelling of bars make the determination of mass quite uncertain even for such models. In fact even the full amount of information one can obtain today for external galaxies, namely the full line-of-sight velocity distribution (LOSVD) at every position on the sky, is not sufficient to uniquely constrain the two free parameters (M/L and inclination) of a simple self-consistent axisymmetric model (Valluri et al. 2004; Krajnović et al. 2005; Cappellari et al. 2006; van den Bosch & van de Ven 2009). A barred model requires at least two extra parameters (the Position Angle (PA) and pattern speed of the bar) and dramatically in-

⋆ E-mail:plablanc@eso.org
† Dunlap Fellow

creases the complexity of the orbital structure and the associated degeneracy of the problem, instead of improving the accuracy of the mass estimate: a broad range of parameters space may well fit the data equally well. Moreover, assuming a galaxy is barred also increases the degeneracy in the mass deprojection problem (e.g. Gerhard 1996), which is already mathematically non unique in the simple axisymmetric case (Rybicki 1987). The application of sophisticated barred models to large samples would be computationally challenging, but feasible exploiting the trivial parallelism of the problem. However, this brute-force approach does not remove the intrinsic degeneracies so it is not expected to increase the accuracy of the mass determinations, and for this reason does not seem justified.

An alternative approach consists of using some a priori information on the galaxy structure and make empirically-motivated restrictive assumption on the models. This is the approach we are using in the systematic determination of the masses of the 260 early-type galaxies of the ATLAS³ᴰ survey (Cappellari et al. 2012). We are applying the Multi-Gaussian Expansion (MGE) technique (Emsellem et al. 1994a) to accurately describe the photometry of all galaxies in the survey (Scott et al. in prep) and use the Jeans Anisotropic MGE (JAM) modelling method (Cappellari 2008) to measure masses. The JAM method is based on a simple and very efficient solution of the Jeans equations which allows for orbital anisotropy $\beta_z = 1 - (\sigma_z/\sigma_R)^2$. This approach provides good descriptions of the integral-field kinematics of the fast rotator early-type galaxies (Cappellari 2008; Scott et al. 2009; Cappellari et al. 2012), which constitute the large majority of the ATLAS³ᴰ sample (see Paper II and Paper III). A key motivation for our use of the JAM method is that it was shown, using 25 real galaxies (Cappellari et al. 2006; Cappellari 2008), to agree well within the model uncertainties in the mass determination obtained with the more general axisymmetric Schwarzschild approach.

The use of an axisymmetric dynamical modelling method to measure the mass of barred galaxies raises the obvious question of what errors in the mass determination are introduced by the approach. Answering this question is the goal of this paper. Our work is in its spirit an extension to barred disk galaxies of the work by Thomas et al. (2007) , which explored the biases introduced by the use of axisymmetric models, when extracting masses of triaxial and prolate simulated spheroidal galaxy remnants.

The paper is structured as follows: in Section 2 we briefly describe the Multi-Gaussian Expansion parametrization from Emsellem et al. (1994a), the semi-isotropic Jeans equations and the method used to create the N-body galaxy models. In Section 3, we give an overview of the input models used for the JAM modeling in our investigation, and in Section 4 we compare the original and recovered values of the corresponding dynamical parameters. Section 5 summarizes all results.

2 MODELING AND N-BODY SIMULATIONS OF EARLY-TYPE BARRED GALAXIES

2.1 Mass modeling

2.1.1 *Multi-Gaussian Expansion method*

We use in our study the Multi-Gaussian Expansion method described in Emsellem et al. (1994a) and Cappellari (2002). The technique basically consists of decomposing the luminosity into a number of concentric two-dimensional (2D) Gaussians. By fitting the detailed surface brightness distribution, the MGE formalism pro-

vides a description of the intrinsic luminosity density, which converts to the mass distribution via the assumed constant M/L. From galaxy images this formalism allows us to generate realistic initial conditions for our N-body simulations using the method explained in Sec 2.3. The MGE parametrization is also the first and crucial step of the JAM modeling. Thus, a rigorous and robust approach is needed when producing the MGE model of a galaxy, as the predicted kinematics may significantly depend on the obtained mass distribution (see Sec 2.2). The method and software[1] we adopt in our study to produce MGE parametrization is fully described in Cappellari (2002).

Once the best fit has been found, we have a description of the galaxy surface brightness distribution given as a sum of two-dimensional Gaussians which we can attempt to deproject. The deprojection of a galaxy surface brightness distribution is formally non-unique for all but edge-on cases, and the degeneracy can become severe at low inclinations (Rybicki 1987). The MGE method provides just *one* solution for the deprojection, in terms of a sum of three-dimensional Gaussians. This method has been intensively used and usually provides luminosity distributions consistent with observed photometry of existing galaxies, but the MGE method obviously does not remove the existing intrinsic degeneracy.

The deprojection of an MGE model can be done analytically once the viewing angles are known (see Monnet et al. 1992). When the system is assumed to be axisymmetric, only one viewing angle, the inclination i ($i = 90°$ for an edge-on system), is sufficient to retrieve the full three-dimensional luminosity distribution ν (if the galaxy is not face-on).

In a coordinate system (x', y', z') centered on the galaxy nucleus with z' pointing toward us and (x', y') being the plane of the sky, the MGE surface brightness can be written as:

$$\Sigma(x', y') = \sum_{k=1}^{N} \frac{L_k}{2\pi \sigma_k'^2 q_k'} \exp\left[-\frac{1}{2\sigma_k'^2} \left(x_r'^2 + \frac{y_r'^2}{q_k'^2} \right) \right] \quad (1)$$

where N is the number of adopted gaussian components, each having an integrated luminosity L_k, an observed axial ratio $0 \leqslant q_k' \leqslant 1$, a dispersion σ_k' along the major axis, and a position angle (PA) ψ_k measured counter-clockwise from y' to the major-axis of the Gaussian, with (x_r', y_r') being the associated rotated coordinate system. Then, the deprojected MGE luminosity distribution in cylindrical coordinates can be expressed as:

$$\nu(R, z) = \sum_{k=1}^{N} \frac{L_k}{(\sqrt{2\pi}\sigma_k)^3 q_k} \exp\left[-\frac{1}{2\sigma_k^2} \left(R^2 + \frac{z^2}{q_k^2} \right) \right] \quad (2)$$

where the k-th gaussian has the total luminosity L_k, intrinsic axial ratio q_k and dispersion σ_k (In the present study $\sigma_k = \sigma_k'$) The intrinsic axial ratio q_k can then be written as

$$q_k^2 = \frac{q'_k{}^2 - \cos^2 i}{\sin^2 i}, \ \text{for} \ i \neq 0 \quad (3)$$

where i is the galaxy inclination.

2.1.2 *MGE modeling of barred and unbarred S0 galaxies*

The fitting of the MGE to the photometry follows the procedure applied by Scott et al. (2009) (see their Fig. 2) to deal with the presence of bars. This same approach is being applied to the MGE fits

---

[1] available from http://purl.org/cappellari/idl
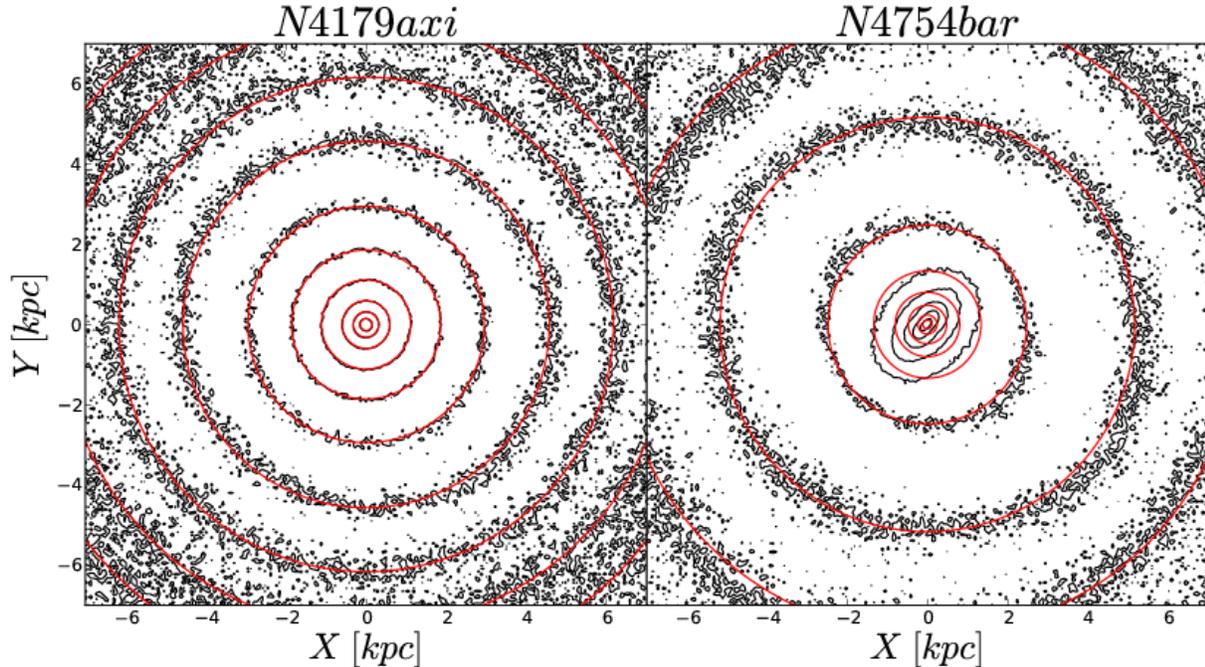
Figure 1. Examples of MGE fits to two model galaxies with a projection angle of $i = 25°$. The left panel shows the MGE fit to simulated galaxy N4179axi, an axisymmetric object. On the right we show the fit to N4754bar with $PA_{bar} = 60°$, where the bar was excluded from the fit.

of the ATLAS^{3D} sample (Scott et al. in preparation). The procedure allows to find the best fit to the photometry, maximizing the minimum q'_k and minimizing the maximum q'_k, while still being consistent with the projected galaxy image within the errors. For near face-on cases, a small deviation in the observed axis ratios implies an important change in the flatness (or roundness) of the mass distribution. As the previous procedure frequently ends with very similar lower and upper limits for q'_k, we force a common axis ratio for all Gaussians for such cases to keep an acceptable global shape for our MGE model.

When the bar clearly affects the projected photometry of our models (i.e., when it is easily detected), the method adopted for the MGE parametrization consists in forcing the lower and upper limit of the gaussian axis ratios. In this context, a bar can be considered as a perturbation of a disk structure. Bars, if fully fitted by MGE components, appear as Gaussians elongated along the apparent long axis of the bar. The presence of a bar tends to significantly affect the q'_k values of a few Gaussians depending on its position angle, strength and length (the position angle of the bar PA_{bar} being measured counter-clockwise from the projected major-axis of the galaxy). The resulting q'_k could thus make the system look flatter (or rounder) than the corresponding axisymmetric case if the bar is seen end-on (resp. side-on). Previous tests made in Scott et al. (2009) showed that the best fitting MGE parametrization of a barred galaxy is usually not the one which allows the best fit to the observed kinematics (using JAM models). The kinematic fit is significantly improved when the Gaussians have constrained axial ratios such that the systems is forced to an axisymmetric "bar-less" MGE parametrization. As bars often only affect the photometry within a restricted radial range, we use the outer disk of each galaxy to constrain the imposed value of the Gaussian flattening. Figure 1 gives

two examples of the resulting MGE fits for an axisymmetric simulation and a barred simulation, **both including large-scale disks**.

2.2 Jeans Anisotropic MGE Modeling

The JAM method is a powerful approach to model the stellar kinematics of early-type galaxies, providing a good description of the first two stellar velocity moments (V, V_{rms}) of a stellar system. This technique can be used to probe the dynamical structure of ETGs and does in principle allow the recovery of the inclination and the dynamical mass-to-light M/L ratio. The JAM technique allows for a different M/L and anisotropy for each individual MGE Gaussian component. However, the measurement of a global mass for real galaxies does not seem to require this extra generality, at least within $1R_e$, where good quality integral-field data are available (e.g. Emsellem et al. 2004, and Paper I). For this reason the models we use make the following simple assumptions (a full description of JAM is provided in Cappellari 2008):

(i) An axisymmetric distribution of the mass.
(ii) A constant mass-to-light M/L ratio.
(iii) A constant anisotropy described by the classic anisotropy parameter $\beta_z = 1 - (\sigma_z/\sigma_R)^2$ with $\beta_z \gtrsim 0$.

When the mass distribution is represented via an MGE parametrization (see Sect. 2.1 above), the Jeans equations can be easily integrated along the line-of-sight as shown by Emsellem et al. (1994a) in the semi-isotropic case ($\sigma_z = \sigma_R \neq \sigma_\phi$) and by Cappellari (2008) in the anisotropic generalization ($\sigma_z \neq \sigma_R \neq \sigma_\phi$). Here we use the anisotropic formulas (equations 28 and 38 of Cappellari (2008)) to derive the projected first and second velocity moments (V and V_{rms}) given a set of input parameters (MGE mass

Model	Galaxy/Model	Distance (Mpc)	N_*	β_{zi}	β_{zf}	σ_ϕ/σ_R	time(Gyr)	bar
N4179axi	NGC4179	16.5	4e6	$\beta(\varepsilon)$	0.106	1.8	1.5	no
N4570axi	NGC4570	17.1	4e6	0.0	0.145	1.0	1.5	no
N4442bar	NGC4442	15.3	4e6	$\beta(\varepsilon)$	0.344	1.8	1.5	yes
N4754bar	NGC4754	16.1	4e6	$\beta(\varepsilon)$	0.343	1.8	1.5	yes

Table 1. Table providing a list of simulations with their labels and their specifications. Distances are set according to Paper I. N_* is the number of particles. β_{zi} gives the anisotropy of the initial conditions as described in Section 2.3.2. β_{zf} is the global anisotropy computed for the final state of our simulations. σ_ϕ/σ_R gives the second relation for the geometry of the velocity dispersion ellipsoid for the initial conditions. The time given in the eighth column correponds to the simulated time of evolution. The last column indicates whether a bar appeared or not in our simulations.

Model	Galaxy/Model	q	Dist	N_*	β_{zi}	$\frac{\sigma_\phi}{\sigma_R}$
Hern01	Hernquist	1.0	10.0	2e6	0.0	1.0
Hern02	Hernquist	1.0	10.0	2e6	0.2	1.0
Hern03*	Hernquist(flat)	0.5	10.0	2e6	0.0	1.0
Hern04*	Hernquist(flat)	0.5	10.0	2e6	0.2	1.0
N4754ini	NGC4754	0.4-0.2	16.1	4e6	0.2	1.0

Table 2. Table providing a list of the tests simulations (static models) with their labels and their specifications. Distance (in Mpc) of $N4754ini$ was set according to Cappellari (2011), while for Hernquist models it was set arbitrary. The flattening of the models is given through the axis ratio q of the MGE models (for N4754ini axis ratio cover a range from $q = 0.4$ for inner gaussians to $q = 0.2$ for outer ones). N_* is the number of particles. β_{zi} gives the anisotropy of the initial conditions as described in Section 2.3.2. σ_ϕ/σ_R gives the second relation for the geometry of the velocity dispersion ellipsoid for the initial conditions.

model, mass-to-light ratio M/L, anisotropy β_z), and thus find the best fitting values within a sampled predefined solution space (e.g., $\beta_z \geqslant 0$)

Such a JAM method has been systemically applied to SAURON integral-field stellar kinematics of all 260 early-type galaxies of the ATLAS$^{\mathrm{3D}}$ sample. In the present study, we rely on mock observations computed from N-body simulations of galaxies, and we chose to build JAM models from artificial maps to mimic the procedure used in the course of the ATLAS$^{\mathrm{3D}}$ survey. We also exclude the central few arcseconds during the fitting process, which e.g., avoids biases due to the effect of the seeing. We also re-bin all maps before fitting by using the Voronoi tessellation as described in Cappellari & Copin (2003): this allows a guaranteed minimum signal-to-noise ratio in each bin, and reduces the scatter in the outer parts of the kinematic maps.

2.3 N-body simulations of regular-rotator galaxies

As the main motivation of our study is to find the influence of a bar on the recovery of basic dynamical parameters with the JAM method, we chose to use an N-body approach to generate simulations of barred early-type galaxies: knowing the exact input dynamics for these simulations, we can then compare the key parameters with those determined via the JAM modeling. We also made static realisations of a few (Hernquist and one typical axisymmetric lenticular) mass models, and thus only used the initial realisation of the N-body distribution. These models are detailed in Table 2, while details for evolved simulations are summarized in Table 1. The method to build the initial conditions for our simulations (to be evolved, or not) is detailed below.

2.3.1 Particle positions

Starting from the MGE parametrization of a mass distribution (after taking into account the mass-to-light ratio M/L), the initial positions of the particles can be computed easily. Each Gaussian represents a fraction of the total mass, so that given a total number of particles per component we can determine N_k, the number of particles of that k-th Gaussian. All components are truncated at a chosen radius. To set up the position of each particle, we use a standard realisation method with a random generator via the cumulative function of a (truncated) Gaussian function, scaling each spatial dimension with the corresponding spatial dispersion.

2.3.2 Dynamical structure

Given the particle position, we compute the velocity dispersion components σ_R, σ_ϕ and σ_z solving Jeans Equations (Jeans 1922), within the MGE formalism of Emsellem et al. (1994a). For this work we use the anisotropic generalization of the method (equations 19–21 and 34 of Cappellari (2008)), which allows one to set arbitrary ratios σ_z/σ_R and σ_ϕ/σ_R for the axes of the velocity ellipsoid, which is assumed to be cylindrically oriented. Values for these ratios can be set individually for each gaussian component, but in this study all Gaussians share the same geometry of its velocity dispersion ellipsoid. For some of the simulations initial conditions, we used the following (so-called $\beta - \epsilon$, with ϵ the intrinsic galaxy ellipticity) relation to fix σ_R/σ_z:

$$\beta_z = 1 - \left(\frac{\sigma_z}{\sigma_R}\right)^2 = 0.6 \times \epsilon \qquad (4)$$

This a purely empirical relation which seems to describe the general trend in the anisotropy of real fast rotator galaxies (Cappellari et al. 2007).

2.3.3 Simulation code

The numerical simulations are performed with a particle-mesh N-body code (Bournaud et al. 2007). The density is computed with a Cloud-in-Cell interpolation, and an FFT-based Poisson solver is used to compute the gravitational potential, with a spatial resolution and softening of 48 pc. Particle motions are integrated with a leap-frog algorithm and a time-step of 0.1 Myr. The number of particles and the time evolution of each model are given in Table 1.
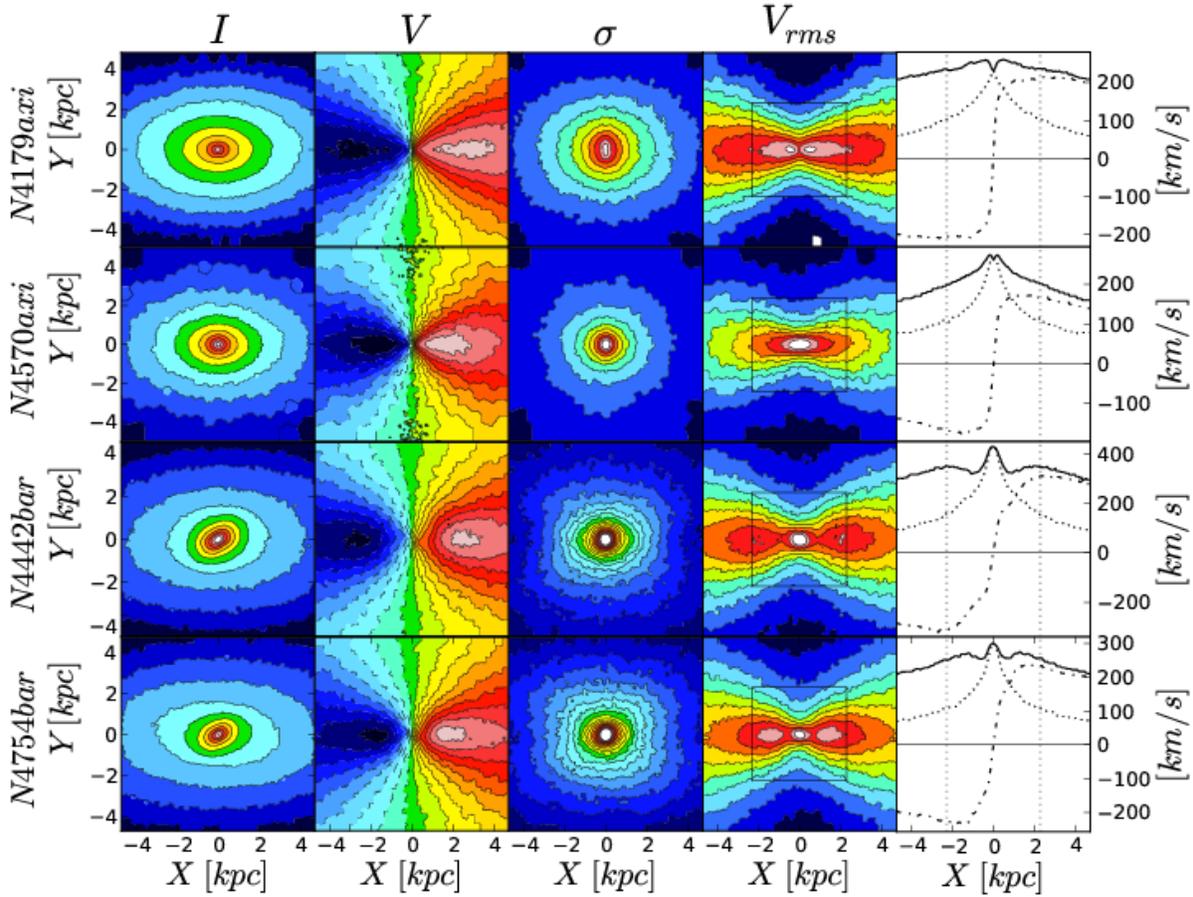
Figure 2. Binned map of the projections of the final state of our simulations with an inclination $i = 60°$ and $PA_{bar} = 60°$ for barred simulations. From left to right : total projected luminosity I ; mean velocity along the line-of-sight V_{LOS} ; velocity dispersion along line-of-sight σ_{LOS} ; projected second velocity moment $V_{rms} = \sqrt{V_{LOS}^2 + \sigma_{LOS}^2}$; profiles of V_{LOS} (dot line), σ_{LOS} (dash-dot line) and V_{rms} (solid line) along the galaxy major axis. From top to bottom : $N4179axi$; $N4570axi$; $N4442bar$; $N4754bar$.The square box in the V_{rms} map and the vertical dot lines in the profiles represent the typical field of view used in our study.

3   INPUTS FOR JAM MODELS

3.1   Unbarred simulations

We first built four simple simulations based on the analytic Hernquist (1990) mass distribution

$$\rho(r) = \frac{M}{2\pi} \frac{a}{r} \frac{1}{(r+a)^3} \qquad (5)$$

where M is the total mass and a is a scale length. These simulations allowed us to quickly check the purely numerical accuracy of the JAM modeling method and of our starting-conditions generating software for spherical isotropic ($Hern01$), spherical anisotropic ($Hern02$), flat isotropic ($Hern03$) and flat anisotropic ($Hern04$) particle realisations. Flat Hernquist models are oblate systems derived from the Hernquist profile by forcing an axis ratio of 0.5 for the mass distribution. For all these simulations the inclination was recovered within an error of less than $2°$ (besides the case of $Hern01$, for which the inclination is meaningless), the global anisotropy was accurately recovered within an error of ±0.025 and the error on M/L never exceeded 1.5%

We then considered a more realistic numerical test, using the MGE parametrization of the SDSS r-band image of the real galaxy NGC4754 and a constant anisotropy and we label this model $N4754ini$. When computing the particle velocities, we forced $\beta_z = 0.2$ for all Gaussians. In contrast to the above-mentioned Hernquist models, $N4754ini$ represents a complex multi-component object in terms of its mass distribution and kinematics, and is therefore expected to be more challenging for the JAM modeling method.

We also built two simulations, respectively based on the MGE parametrizations of NGC4570 and NGC4179, which were evolved via N-body simulations during 1.5Gyr (the face-on and edge-on projections of the final state are illustrated in A1). These two simulations can be considered as fully relaxed, and contrarily to $N4754ini$ and the Hernquist models, the resulting β_z is measured not to be constant with radius. One important difference between $N4570axi$ and $N4179axi$ is that, while the initial conditions for $N4570axi$ were fixed as isotropic ($\beta_z = 0$), the ones for $N4179axi$ were those of a dynamically cold disk as described in Table 1. No bar formed either for $N4179axi$ or $N4570axi$.

Projected velocity and velocity dispersion maps of our two axisymmetric simulations with variable β_z are presented in Figure 2. The second velocity moment is dominated by the dispersion in the central region, and by the velocity in the outer parts. The profile of $V_{\rm rms}$ also shows a central depletion.

Figure 3 present the local anisotropy β_z as measured in the meridional plane and the equatorial plane, computed on a cylindrical grid with linearly spaced cells in R, in z and in angle ϕ where (R,ϕ,z) are the standard cylindrical coordinates, including a central cylindrical cell with a radius of $R_c = 0.01$kpc. This highlights the fact the anisotropy is not constant in our axisymmetric simulations and that the central parts are more isotropic than the outer regions. In Figure 4, we show that the radial anisotropy profile (which is simply the azimuthal average of the equatorial computation) generally increases outwards for these axisymmetric simulations.

3.2 Barred simulations

We also developed bar simulations, $N4442bar$, and $N4754bar$, based on the initial MGE parametrizations of NGC4442 and NGC4754, respectively: these are the final state of two N-body simulations after 1.5 Gyr of evolution (face-on and edge-on projections of the final state can be found in A1). To generate a bar, we force a cold dynamical structure in the initial particle realisations by setting in the initial conditions $\sigma_\phi = \sigma_R/1.8$. The radial velocity dispersion σ_R was set using the $\beta(\varepsilon)$ function described in Eq. 4. With these conditions, a bar appears in each of these simulations after only a few rotation period, namely between about 25 Myr and 50 Myr of simulated evolution. As mentioned, we let the galaxy evolve for 1.5 Gyr, to make sure that the bar is well settled.

$N4442bar$ presents the biggest bar (in size) of our simulations: we estimate a semi-major axis of 3.0 kpc. The size of the bar is determined using the radial flattening ($q_{isophote} = 1 - \epsilon_{isophote}$) and the position angle ($PA_{isophote}$) of isophotes as done in Michel-Dansac & Wozniak (2006). Basically we define the end of the bar as the radius where isophotes are nearly round ($q_{isophote} > 0.9$) combined with an important change in the position angle. Using the same method we determine the semi-major axis of the bar for $N4754bar$ to be 2.2 kpc. Outside of the bar regions, our two simulations are characterized by a rotation pattern consistent with an axisymmetric disk-like system.

The velocity fields of our barred simulations are shown in the two lower panels of Figure 2. As for the axisymmetric cases, the $V_{\rm rms}$ maps are dominated by velocity dispersion in the central parts and by the mean velocity in the outer parts. But in contrast to the $N4179axi$ and $N4754ini$ simulations, the barred simulations all show a peak in the center of the $V_{\rm rms}$ maps. This apparent difference between the barred and unbarred cases has important consequences, since this will condition the fit of the projected second velocity moment via a JAM model.

Figure 3 and Figure 4 show that the local anisotropy starts from a central value of 0.3, reaching a minimum of nearly 0.2 close to the end of the bar, then increasing in the outer parts of the model up to 0.7. The derivation of β_z in the equatorial plane confirms the presence of a drop in β_z in the outer parts of the bar.

3.3 Mock observations

As input for the JAM modeling, we simulated observations by projecting our simulations first with four different inclinations: $i = 25°$; $i = 45°$; $i = 60°$ and $i = 87°$, ($i = 0°$ corresponding to the face-on projection, and $i = 90°$ to the edge-on projection). The choice
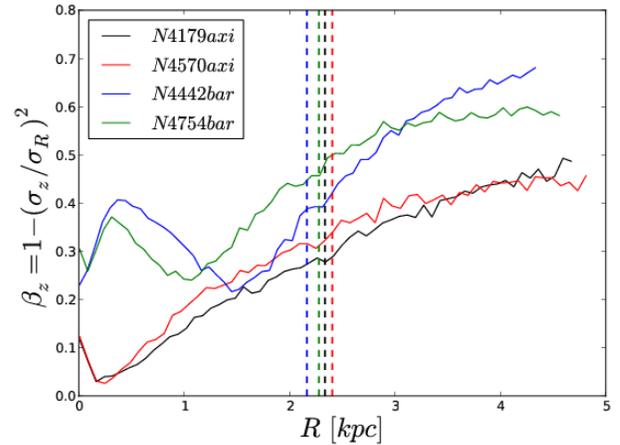
Figure 4. Azymuthally averaged profile of the anisotropy computed in an equatorial plane ($-0.5kpc < z < 0.5kpc$) for axisymmetric simulations ($N4179axi$ and $N4570axi$) and barred simulations ($N4442bar$ and $N4754bar$). The vertical dash-dot lines correspond to the field of view used for the JAM models and therefore the region in which we derived the global anisotropy.

of a near edge-on projection instead of an exact edge-on projection was motivated by the goal of checking the accuracy of the inclination recovery. Indeed the edge-on projection does not allow an overestimation of i and then limits the range of possible uncertainty. When a bar is present, we also used four different position angles for the bar, and this for each value of the inclination: $PA_{bar} = 18°$; $PA_{bar} = 45°$; $PA_{bar} = 60°$ and $PA_{bar} = 87°$. The position angle of the bar is measured counter-clockwise from the galaxy projected major-axis to the bar major-axis, so that $PA_{bar} = 87°$ is close to having the bar end-on and $PA_{bar} = 18°$ close to side-on. We also simulated the SAURON pixels size of $0.''8$ assuming a distance for each model as given in Table 1 typical of ATLAS^{3D} objects. **Note that the M/L provided in Table C1 could have been chosen as unity, considering that we will only probe here relative M/L. However, we favoured realistic values as to deal with sensible velocity measurements.**

For real galaxies the photometry is available over a much larger field of view than the kinematics. For each projection, the MGE parametrization was achieved using a rather wide field of view of 401×401 pixels corresponding to 320.8 arcsec, and including the full model. Then, the JAM modeling was fit on a 73×73 pixels map (58.4 arcsec) of the second velocity moment with the simulated galaxy centered on its nucleus, as this roughly corresponds to the setup for a single SAURON exposure.

4 RECOVERY OF PARAMETERS

The recovery of i, β_z and M/L with JAM is done on $V_{\rm rms}$ maps only. The prediction of V and σ require an extra assumption on the constancy of the tangential anisotropy of the JAM models. This assumption may not be well verified in the simulations, especially in barred ones. However, the accuracy in the determination of the above parameters only depends on the ability of JAM to reproduce the $V_{\rm rms}$, and not the V and σ fields separately. Details of the method to calculate V and σ can be found in Cappellari (2008).
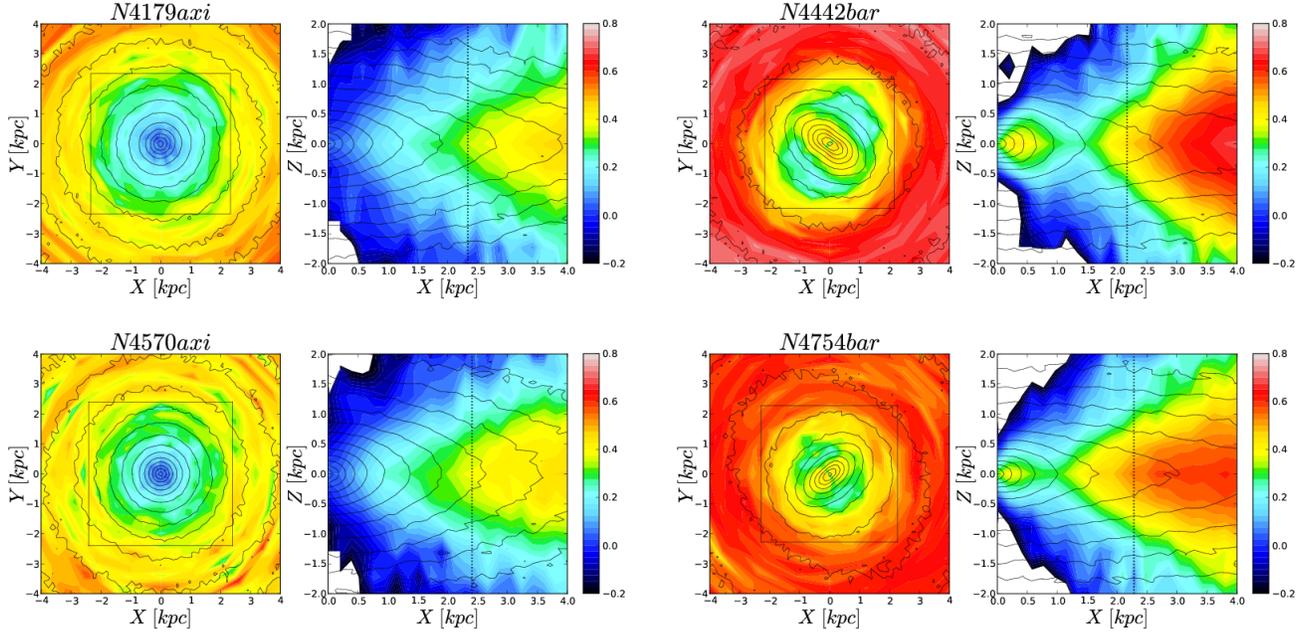
Figure 3. Maps of the local values of the anisotropy β_z in the equatorial plane and in the meridional plane of $N4179axi$ (upper left), $N4570axi$ (bottom left), $N4442bar$ (upper right) and $N4754bar$ (bottom right). Colour gradients for the anisotropy go from $\beta_z = -0.2$ (i.e. $\sigma_z > \sigma_R$) to $\beta_z = 0.8$ (i.e. $\sigma_z < \sigma_R$). The field of view used in our study is represented by the solid square for the equatorial plane and by the vertical dot line for the meridional plane.
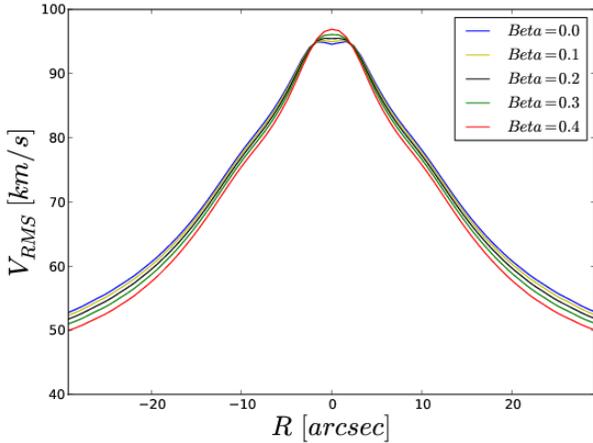
Figure 5. Effect of the anisotropy parameter β_z on the observed $V_{\rm rms}$ profile along major axis at an inclination of $i = 18°$. The difference between all profiles is too small to allow a good recovery of β_z at such low inclination.

4.1 Recovery of β_z and inclination

As shown in Figure 4 the anisotropy varies significantly when going from the inner to the outer parts of our simulations.

The JAM modelling method allows for a different anisotropy β_z for every individual MGE Gaussian. Here we limit ourselves to the simple case where β_z is constant for the whole model. Tests using 25 real galaxies (Cappellari et al. 2006; Cappellari 2008) have shown that even with constant anisotropy the recovered M/L agrees with the one derived with Schwarzschild models, which allow for a general anisotropy distribution. The extra generality of JAM is therefore not required in this case. Thus, for comparison,

we compute a global anisotropy for our simulations by doing a luminosity-weighted average of the local anisotropy for all of our simulations. In the following we discuss the issue of the inclination-anisotropy degeneracy intrinsic to galaxy dynamics and also the important influence of the MGE parametrization on the recovery of the global anisotropy. The global anisotropy recovered with the JAM modeling method is noted $\beta_z^{\rm JAM}$ and the one computed directly from the simulation $\beta_z^{\rm SIM}$.

4.1.1 Anisotropy-inclination degeneracy

As shown in Krajnović et al. (2005) and with more galaxies in Cappellari et al. (2006) there is an intrinsic degeneracy in the dynamical problem between the recovery of the inclination and the anisotropy: given the observed photometry, the observed kinematics can be reproduced in detail for a wide range of inclinations, by varying the orbital make up of the models. This degeneracy persists even in the restricted case in which the anisotropy is assumed to be constant for the whole galaxy (Cappellari 2008). The degeneracy can only be broken by making empirically-motivated assumptions on the anisotropy. This was the approach adopted by Cappellari (2008), who showed using a small sample of galaxies that, if β_z is assumed to be positive, as determined using general models on large samples of galaxies (Cappellari et al. 2007; Thomas et al. 2009), the correct inclination can be recovered from the observed integral-field kinematics.

Here we test the inclination recovery via JAM using N-body simulations of both unbarred (i.e. $N4179axi$ and $N4570axi$) and in particular barred galaxies (i.e. $N4442bar$ and $N4754bar$), for which the inclination is known. We confirm the fact that, despite the inclination-anisotropy degeneracy the inclination can be recovered in axisymmetric simulations, and we additionally find that the inclination can be recovered even in barred simulations. The influ-
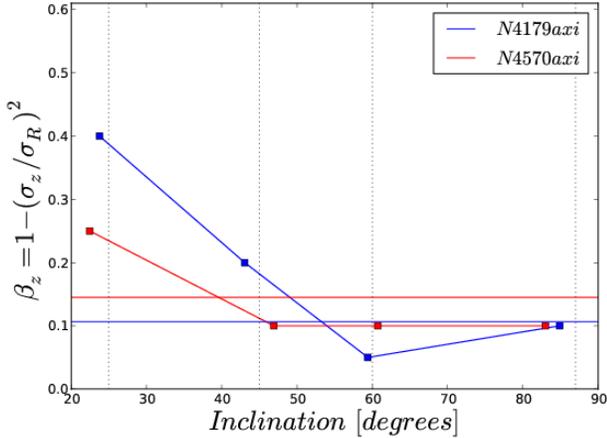
Figure 6. Recovered values of the global anisotropy for non-barred simulations as a function of the projection inclination for $N4179axi$ and $N4570axi$. The horizontal lines represent the global anisotropy computed from the particle realisation β_z^{SIM} (blue for $N4179axi$ and red for $N4570axi$). Vertical lines give the inclination of projections.

ence of i on the second velocity moment map is important at low inclination. A slight change in the inclination implies a significant change in V_{rms} (which is more directly related to the change in the axis ratio), and then allows a good recovery of the inclination value i. At higher inclination, the change in ellipticity is milder and V_{rms} is less influenced by small variations. In all cases, the uncertainty never exceeds a few degrees, even when the fit can be considered difficult due to the presence of non-axisymmetric features such as a bar. We also confirm that at low inclinations ($i \lesssim 40°$) there is a degeneracy in anisotropy in the V_{rms} fit, essentially preventing any information on the anisotropy from being extracted from the data in that case. As shown in Figure 5, changes induced by the anisotropy parameter on the V_{rms} profiles are not significant for $i = 18°$. This is due to the fact that at low inclination, maps of the second velocity moment are dominated by σ_z. Therefore, to avoid a too strong degeneracy, $i = 25°$ is the lowest inclination we will consider in this study. For lower values, the degeneracy prevents β_z from being usefully recovered.

To summarize, the higher the inclination, the larger the effect of the global anisotropy on the projected V_{rms}. For the non-barred simulations, following eight different projections (2 galaxies projected at 4 inclinations), we find average errors of 2 degrees and maximum error of 4 degrees at an edge-on view, where the deprojected axial ratio changes most weakly with inclination. For the barred simulations (32 determinations: 2 galaxies projected at 4 inclinations and 4 PA$_{\mathrm{bar}}$) the maximum error in the recovered inclination is 6 degrees. The maximum error happens only for PA$_{\mathrm{bar}} \sim 90°$, when the bar is seen side-on and it is incorrectly deprojected as a thin disk (see Fig 8). The error on β_z^{JAM} is important at low inclination and decreases from face-on to edge-on projections.

4.1.2 Influence of the mass deprojection

While the inclination-anisotropy degeneracy is intrinsic to the galaxy dynamics and determines the uncertainties for the recovered global anisotropy and the inclination, β_z^{JAM} is also influenced by the mass deprojection. For regular axisymmetric simulations such

as $N4179axi$ and $N4570axi$, the MGE parametrization is relatively robust, and β_z^{JAM} is generally very close to the known intrinsic value β_z^{SIM} (see Figure 6). The deviations near face-on view are due to the degeneracy in the mass deprojection at that low inclination.

For the barred simulations $N4442bar$ and $N4754bar$, the presence of the bar implies that axisymmetric models cannot reproduce the true stellar density distribution. This means that our MGE parametrization can only provide an approximation. Fig 7 and Fig 8 illustrate the impact of the degeneracy in the mass deprojection of barred galaxies. The deprojected surface brightness MGE model of a barred galaxy is shown for three inclination of the galaxy ($i = 25°$, $i = 60°$ and $i = 87°$) and two positions of the bar ($PA_{bar} = 18°$ and $PA_{bar} = 87°$). Close to edge-on ($i = 87°$, bottom panels), the reconstructed deprojected models do a reasonable job at fitting the true edge-on surface brightness contours. When the bar is close to end-on, the impact of assuming an axisymmetric model becomes more visible. At the other extreme end, near face-on models ($i = 25°$, top panels) have deprojected contours which significantly depart from the true edge-on ones. This is mostly due to the fact that a small change in the fitted axis ratio of the Gaussians has a large impact on the intrinsic axis ratio after deprojection : this is further illustrated and emphasised in Appendix B1. For intermediate viewing angles ($i = 60°$, middle panels), the deprojected photometry fits reasonably well the true edge-on contours, while again, the discrepancy is emphasised in the region of the bar when it is initially viewed edge-on. For a real, observed near face-on galaxy, it is hard to know how close the MGE fitting process would get from the intrinsic axis ratio of the outer disk, as it would depend on e.g., the regularity of the disk (for example, its lopsidedness), the signal to noise and contamination from the sky. but Fig 7 and Fig 8 demonstrate that a significant degeneracy exists when deprojecting targets at low inclination (close to face-on). These tests show that, as expected, (i) the presence of a bar produces a deprojected density flatter (rounder) that the azimuthally averaged one when the bar is close to side-on (end-on), (ii) near a face-on inclination the deprojected density can be significantly in error. This obviously impacts the associated dynamical modelling, as detailed in the following Sections.

The results presented in Figure 9 are obtained by applying the same method used on observations. We can see that the global anisotropy is never well recovered. This is explained by the fact that the presence of the bar will tend to flatten or round the Gaussians in the MGE parametrization if it is seen respectively side-on ($PA_{bar} = 18°$) or end-on ($PA_{bar} = 87°$). It is important to note that this bias, being due mainly to the mass deprojection (see Fig 7 and Fig 8), is not specific to the adopted dynamical modelling method, but is expected to affect more general method like Schwarzschild's orbit-superposition method. Moreover the anisotropy is formally not a well defined quantity in a barred galaxy, as it is expected to vary with the azimuthal location on the galaxy disks.

To further investigate the impact of the ellipticity ϵ on β_z^{JAM}, we computed the positions of our mock observations in the (V/σ, ϵ) diagram (Binney 2005). (V/σ) and ϵ are computed in an ellipse of area $A = \pi R_e^2$ where R_e is the radius of a cylinder enclosing half of the galaxy light. In Figure 10 we present the result for near edge-on projections with R going from $0.5 \times R_e$ to $5.0 \times R_e$. We only consider the edge-on case in this figure as all our models follow the inclination law (see Sec. 4.3 of Binney & Tremaine 1987). For comparison additional simple models were also constructed and projected edge-on. The first one (named Test01) is based on a MGE parametrization with constant $\epsilon = 1 - q$ and isotropic
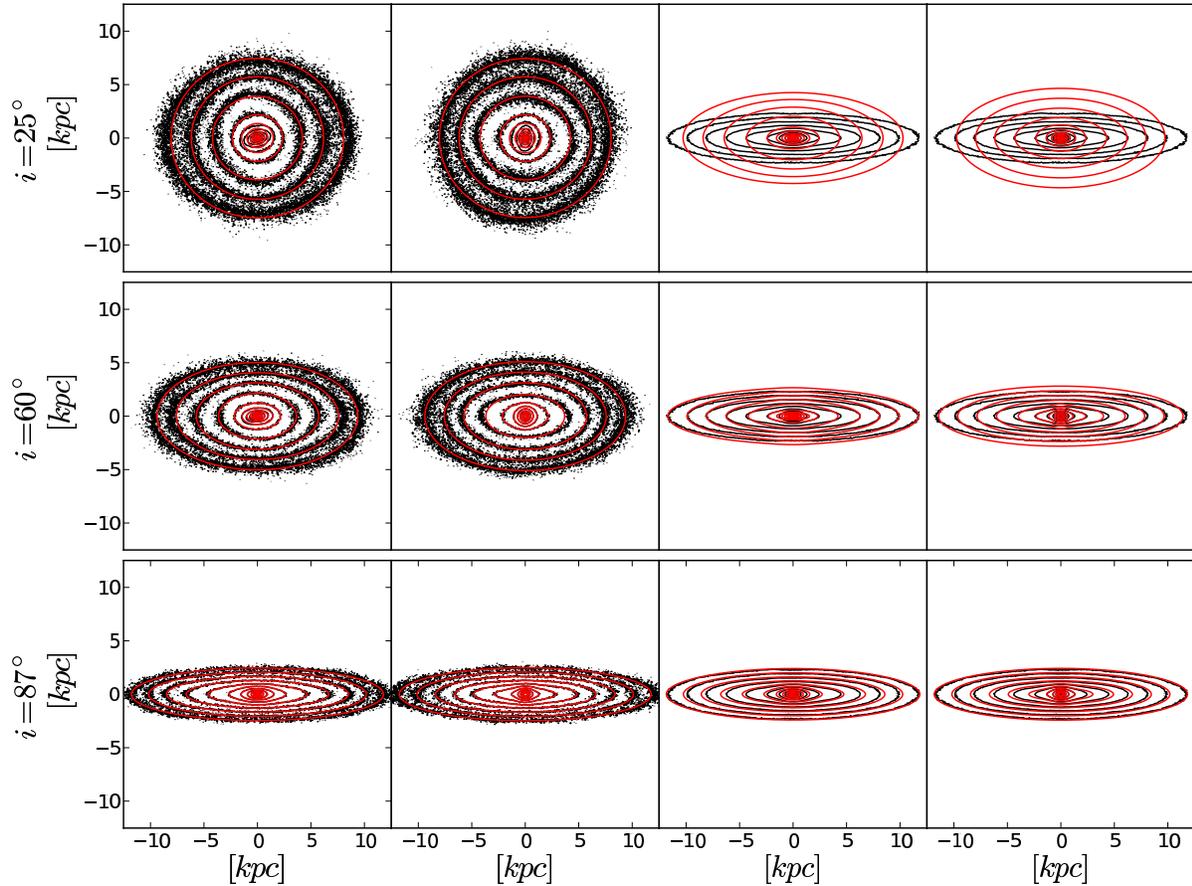
Figure 7. Effect of the inclination on the deprojection of MGE models for $i = 25°$, $i = 60°$ and $i = 87°$. In the first and second columns the MGE fitting (red lines) of the projected mass distribution (black contours) is shown for $PA_{bar} = 18°$ and $PA_{bar} = 87°$. The edge-on deprojections of the two latter MGE fitting are represented in the third and fourth columns respectively, superposed to the azimuthally averaged projected density.

.

kinematics (black solid line on the Figure 10). The second one (Test02) is also isotropic but with a non constant ellipticity in the mass distribution, ϵ increasing with radii (black dashed line).

These two test models highlight the fact that when the considered area A is increased (V/σ) increases as to roughly follow the constant anisotropy lines. The axisymmetric model $N4179axi$ also lay on a constant anisotropy line although its dynamical structure presents a β_z gradient. Barred simulations present a different behavior depending on PA$_{bar}$. With broad field of view (FOV) the only effect of the bar is seen through (V/σ) which decreases when PA$_{bar}$ increases. But when the size of the FOV is of the order of the bar size, ϵ is affected by PA$_{bar}$ and then the projections spread over a wide range of anisotropy. The intrinsic ellipticity of the MGE parametrization plays here an important role for the anisotropy recovery.

We made a second test to better understand the effect of the MGE parametrization on a model of barred object. From the same projection we created two different MGE models : the first one is a "free" model with gaussian axis ratios left unconstrained ; for the second one we forced the maximum and the minimum axis ratio as we do know the intrinsic mass distribution. We did not include here the case PA$_{bar}$ = 45° for which the MGE parametrization

is forced to be neither flatter nor rounder than the axisymmetric case. As expected, when we forced the axis ratio during the MGE parametrization, the global anisotropy β_z^{JAM} recovered was found to be much closer to β_z^{SIM} as shown in Fig 11. We can then assume that the accuracy in the recovery of the global anisotropy is mainly biased by the MGE parametrization of the photometry.

Unfortunately, we cannot always objectively choose the best deprojected model when we apply the JAM modeling method to real observations. And for barred galaxies the accuracy on β_z will only be improved if we can really see the bar or have strong evidence for its presence.

4.2 Recovery of M/L

The Mass-to-Light ratio M/L is the third parameter (after the inclination i and the global anisotropy β_z) computed with the JAM modeling method.

When using the initial conditions, we simply compare the recovered M/L with the input ones. For evolved galaxies we used instead, as our reference, the M/L computed from the direct application of the virial relation $2K + W = 0$ to the simulation particles, where K is the total kinetic energy and W is the total potential
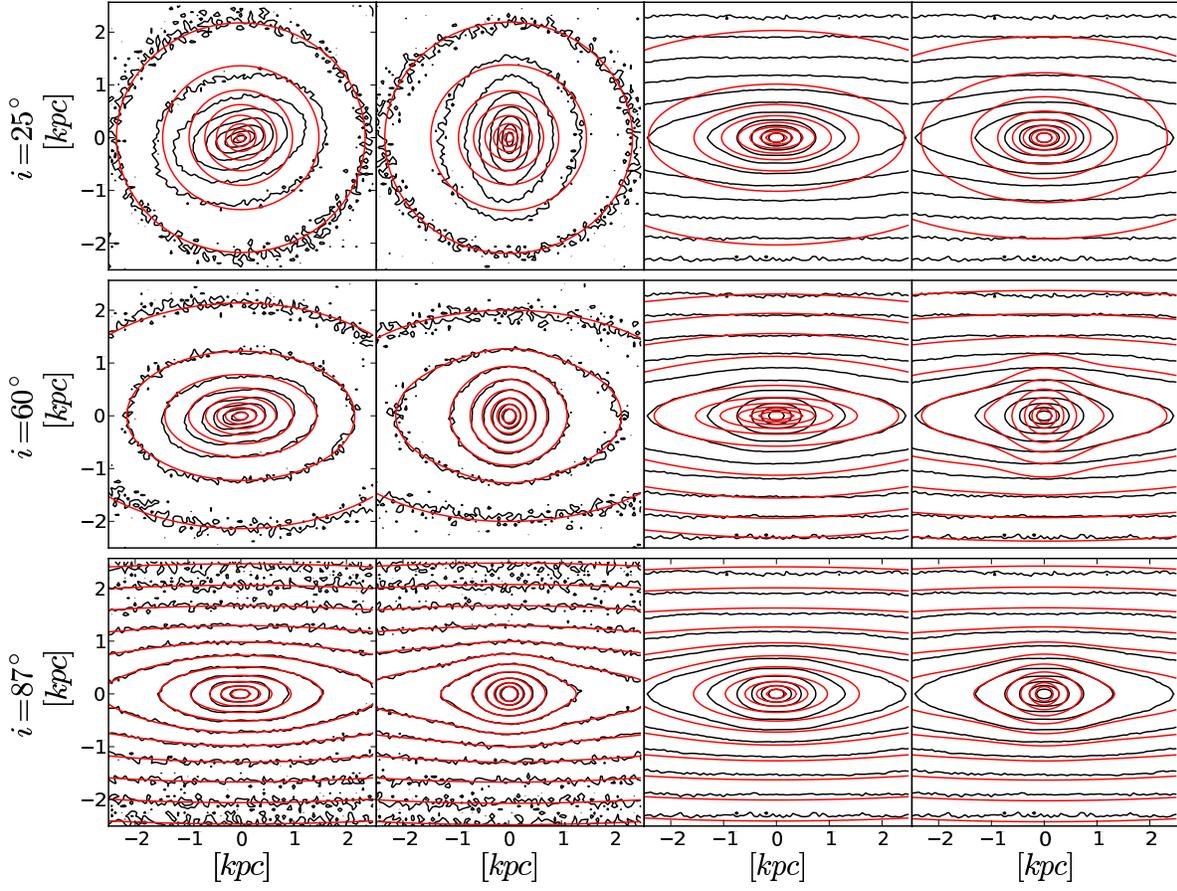
Figure 8. Same as Figure 7 with a field of view of $5kpc \times 5kpc$.
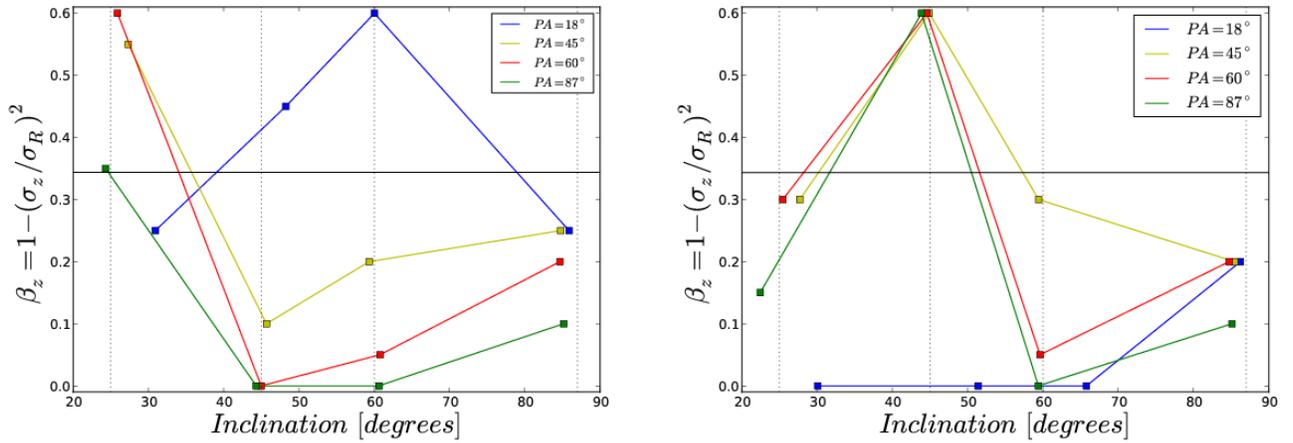
Figure 9. Recovered value of the global anisotropy for barred simulations as a function of the projection inclination for $N4442bar$ (left) and $N4754bar$ (right) for different PA_{bar}. The horizontal black solid line represent the value of β_z^{SIM} and the vertical lines shows the inclinations of projection.

Figure 12. Recovered value of M/L for non barred simulations $N4179axi$ and $N4570axi$ as a function of the inclination of projection. In these regular axisymmetric simulations we find an error of 1.5% on M/L (excluding the near face-on projection).
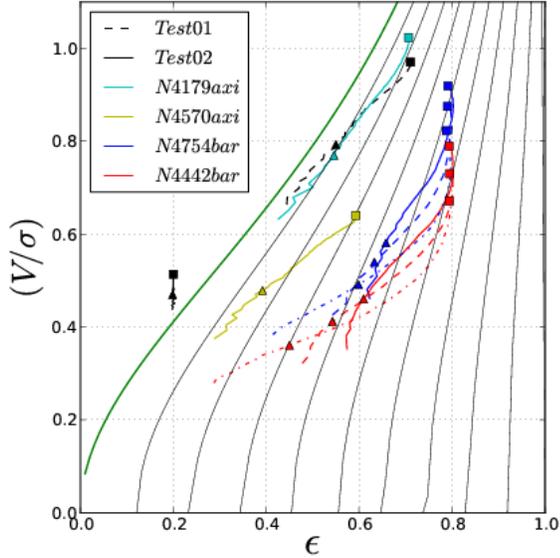
Figure 10. Positions of edge-on projections of all models in the $(V/\sigma, \epsilon)$ diagram. The two tests models described in Section 4.1.2 are in black. The green line and the thin black solid lines correspond to isotropy and constant anisotropy in the diagram with a step of 0.1 from left to right. The cyan line correponds to $N4179axi$; the yellow one to $N4570axi$; the blue ones to $N4754bar$ and the red ones to $N4442bar$. For barred simulations the solid line refers to $PA_{bar} = 18°$; the dashed one to $PA_{bar} = 45°$ and the dash-doted one to $PA_{bar} = 87°$ (we removed the case $PA_{bar} = 60°$ for better legibility). The wider FOV is represented by a square and our reference FOV in the present study by a triangle.
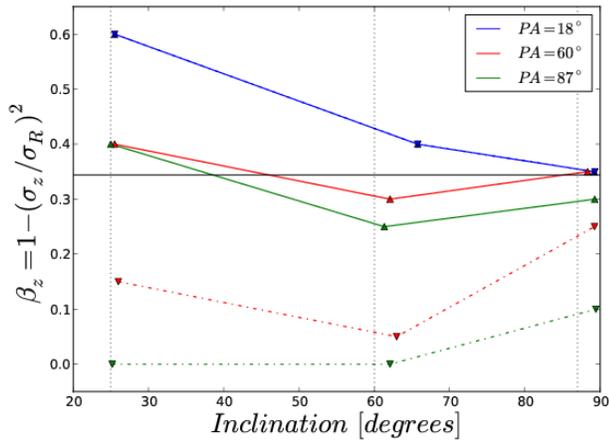
Figure 11. Recovered values of the global anisotropy as a function of the projection inclination for two different MGE parametrization of the same model. The color solid lines are the values recovered with a model with forced axis ratio for the MGE parametrization and the dash-dot lines are for a free MGE parametrization (see Section 4.1.2). Note that the blue solid line and the blue dash-dot line are overlapping. The horizontal black line is the value β_z^{SIM} computed from the model.

energy of our simulations.The relation makes no other assumption that a steady state, and thus provides the natural benchmark against which to compare stationary dynamical models. In general one expects simulations and real galaxies to satisfy the relation quite accurately, so that the virial M/L_{vir} will agree with the input one M/L_{SIM} and no distinction needs to be made. However Thomas et al. (2007) found that M/L_{vir} can differ from the input one at the 5% level, due to non stationarity, and our results agree with theirs. As we are not interested on investigating the stationarity of the model, but only the biases of the modelling method, for maximum accuracy we use as reference M/L_{vir} in all the comparisons which follow.

To probe the robustness of our method we applied it to the four Hernquist particle realisations created from the analytic formula of Hernquist (1990). The results both in the recovery of the global anisotropy and the M/L were excellent, with an accurate recovery of β_z and errors on M/L of less than 1.5%. Whilst these simulations are basic and do not reproduce the complexity of a real galaxy, this is a reassuring test of our machinery.

An intermediate case between simple analytic simulations and real galaxies, is the $N4754ini$ model which is just a regular axisymmetric rotating galaxy with a constant anisotropy. Its mass distribution corresponds to a real galaxy but its intrinsic dynamics are simple, as the velocity anisotropy is set to be constant throughout the galaxy. The global anisotropy is well recovered within 0.025 and the mass-to-light ratio is recovered with an error of less than 1.5%. Although unrealistic, this case helps isolate the influence of a variable anisotropy on the results of the JAM modeling method.

We then used the JAM modeling method on $N4179axi$ and $N4570axi$ to explore any systematic bias that may be present *without* the presence of a bar. Results are shown in Figure 12 and JAM fitting in Fig. D1 and Fig. D2. Figure 12 emphasizes that one can expect significant overestimations of M/L up to $\sim 10\%$, when the galaxy is close to face-on. This important fact is illustrated with an analytic test in Fig. 4 of Cappellari et al. (2006) and with the galaxy NGC0524 in Fig. A1 there. Here we confirm it with the present simulations. In what follows we will focus on the higher inclinations. However, one should keep in mind that the M/L of nearly face-on galaxies has to be treated with caution. For $i = 45°$; $i = 60°$ and $i = 87°$ then, we find that in regular axisymmetric cases M/L is
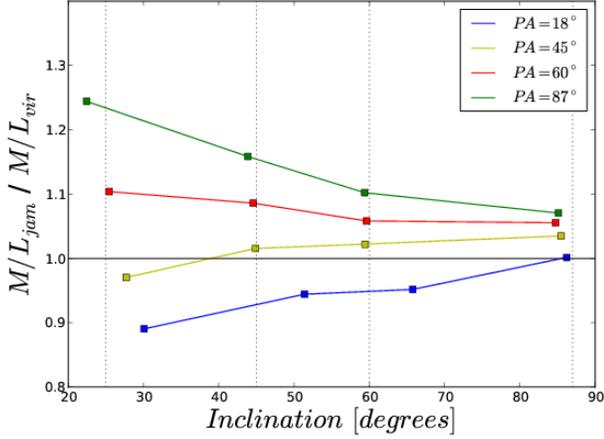
Figure 13. Recovered value of M/L for $N4754bar$ as a function of the projection inclination for different values of $\mathrm{PA_{bar}}$.
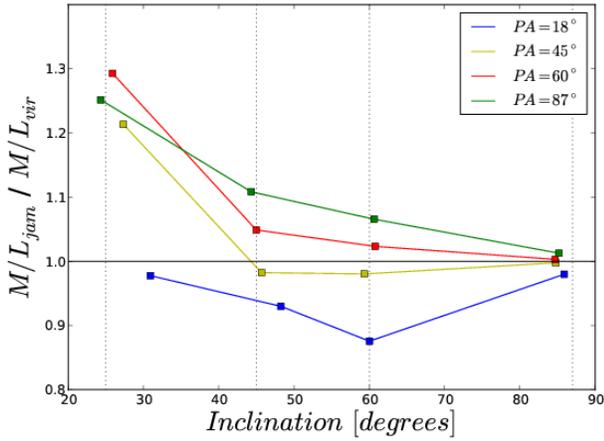
Figure 14. Recovered value of M/L for $N4442bar$ as a function of the projection inclination for different values of $\mathrm{PA_{bar}}$.

recovered with a negligible median bias, and a maximum error of just 1.5%.

Figure 13 and Figure 14 respectively present the results of JAM modeling of $N4754bar$ and $N4442bar$. As for axisymmetric cases, we only consider here inclination projections with $i \geqslant 45°$. For high inclination projections the M/L is recovered within 3% for a $\mathrm{PA_{bar}} = 45°$, which represents the average for random orientations. However the bias in the recovery can reach up to 15% in our tests cases. But the main point is that the recovered M/L is correlated with the position angle of the bar, $\mathrm{PA_{bar}}$. The more the bar is seen end-on, the larger the overestimation, due to the larger velocities of the stars moving along the bar, and towards the line-of-sight, with respect to the other directions in the disk plane. The reason is that the presence of a bar produces a peak in the V_{rms} maps which is not present in the purely axisymmetric case (see Figure 2). In order to fit this peak, the JAM model tend to larger M/L values. Moreover, the amplitude of the peak increases with $\mathrm{PA_{bar}}$, which explains why the value of M/L_{JAM} also increases with the position angle of the bar. The exclusion of the central regions helps to reduce the bias introduced by the bar in M/L_{JAM}, but in cases
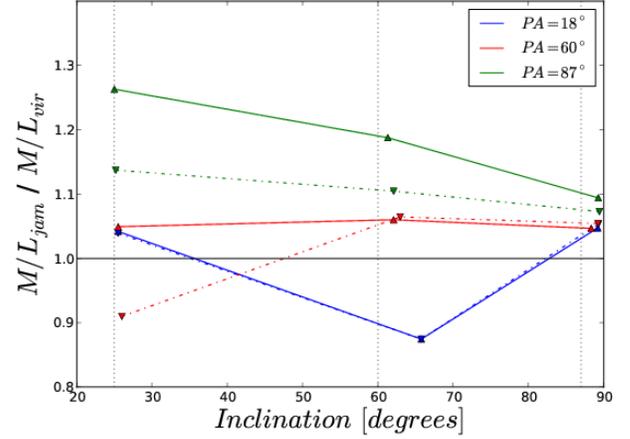
Figure 15. Recovered value of the mass-to-light ratio as a function of the projection inclination. The color solid lines are the values recovered with a model with forced axis ratio for the MGE parametrization and the dash-dot lines are for a free MGE parametrization.

where the bar dominates the whole field of view, we cannot expect to get rid of its influence.

The case when the bar is seen side-on ($\mathrm{PA_{bar}} = 18°$) for $i = 45°$; $i = 60°$ and $i = 87°$ is a special configuration for the mass deprojection. As the flat bar is deprojected as a flattened disk (see Fig 8), following the axisymmetric assumption, the JAM model is unable to reproduce the global shape of the V_{rms} map (see Fig D4-D6, Fig D8- D10 top left panel). The error on the recovered mass-to-light ratio can be up to $\sim 10\%$. In fact the global shape of the V_{rms} map is dictated by the global anisotropy. The mass-to-light ratio essentially adjusts the fit to the global level of the second velocity moment.

The position of the bar $\mathrm{PA_{bar}} = 45°$ is a useful reference, as it represents the average value for random orientations. As previously mentioned in this case the MGE parametrization is hardly affected by $\mathrm{PA_{bar}}$. In this configuration the error on M/L does not exceed 3%, although the V_{rms} map is not reproduced. Basically for projections with $\mathrm{PA_{bar}} < 45°$ M/L is expected to be underestimated while for projections with $\mathrm{PA_{bar}} > 45°$ it is overestimated.

Then for $\mathrm{PA_{bar}} = 60°$ and $\mathrm{PA_{bar}} = 87°$, the bar produces a vertically elongated structure in projection and an artificially round bulge when deprojected as an axisymmetric system. However the reproduction of the V_{rms} shape is still a hard task for the JAM model (see Fig D4- D6, Fig D8- D10 right column). A brief investigation pertaining to the influence of the MGE parametrization on M/L_{JAM}, illustrated by Figure 15, shows that forcing the flattening of the mass distribution in the JAM model does not really affect M/L_{JAM}, except for $\mathrm{PA_{bar}} = 87°$. For this bar position the accuracy in M/L_{JAM} is increased, but at the same time, as previously mentioned in Section 4.1, the accuracy on the recovered global anisotropy is decreased. The prediction of the V and σ fields, are however significantly improved, when forcing q_k, is as already shown in figure 3 of Scott et al. (2009).

To sum up, when a bar is present the M/L overestimation or underestimation with the JAM modelling method are clearly due : (i) to the fact that the mass is incorrectly deprojected as too flat or too round, when the bar is edge-on or side-on respectively ; and (ii) to the fact that the projected second moments are lower or higher when the bar is edge-on or side-on respectively.
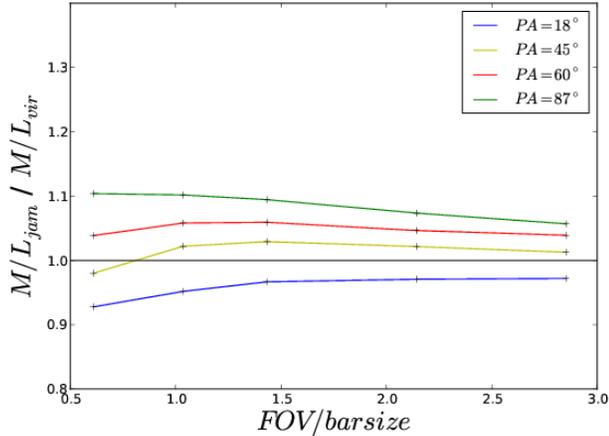
Figure 16. Effect of the FOV on the accuracy of the recovered M/L of $N4754bar$ projected with $i = 60°$. The $x - axis$ correspond to the size of the side of the field of view normalized by the size of the major axis of the bar determined in Section 3.2.

To reduce the effect of the bar, one possible solution is to fit the JAM model only to regions where the bar has little or no influence. We therefore investigated the effect of the size of the field of view (FOV) on $M/L_{\rm JAM}$. One could expect that when increasing the FOV further we could minimize the effect of the bar on the fit and thus reach a better accuracy in the recovering operation. To test this, we increased the FOV of our mock data and repeated the JAM fitting procedure (the MGE parametrization was not affected as it is anyway done on a projection of the simulations with a very large field of view). Figure 16 illustrates $M/L_{\rm JAM}$ as a function of the size of one side of the FOV normalized by the size of the bar for $N4754bar$. We find that, as expected, the FOV plays a role in the recovered values. When the size of the FOV exceeds the bar size $\Delta M/L$ decreases and seems to tend to a limit value. This is expected as we cannot totally get rid of the effect of the bar in the $V_{\rm rms}$ maps. In our study, the typical fitted field of view is quite comparable to the size of the bar itself, meaning that our previous results are close to the worst case scenario. The relative size of the bar with respect to the size of the field of view is an important ingredient for the recovery of the mass-to-light ratio.

To conclude, when modeling a barred galaxy assuming an axisymmetric mass distribution, the M/L is on average (at $PA_{\rm bar} = 45°$) still well recovered. It can, however, be overestimated, when the bar is parallel to the line-of-sight, or overestimated, when the bar is orthogonal to the line-of-sight, by up to 15% (in our tests). The amplitude of these errors mainly depend on the position angle of the bar $PA_{\rm bar}$, but also on the size of the FOV. Excluding the most central parts and increasing the FOV would naturally tend to reduce the influence of the bar without removing the error on M/L entirely.

5 CONCLUSION

This paper focuses on the study of the possible biases in the M/L and anisotropy determination for barred simulations, when using axisymmetric dynamical models. This extends previous studies (Thomas et al. 2007) of triaxial and prolate merger remnants to axisymmetric and barred simulated disk galaxies that better resemble observed fast early-type rotators which constitute the large majority

of the gas-poor population in the nearby Universe (see Paper II and Paper III). We do this by generating N-body simulations of objects with properties similar to observed galaxies, both with and without bars. These are projected at various viewing angles and used to generate mock observations that closely resemble real data. These data are then fed into the JAM modeling machinery as for real data, the difference being that the intrinsic values of the free JAM model parameters (i, β_z, M/L) are known for the simulated data set.

The errors in the recovered inclination increase with inclination due to the fact that, as previously noticed, the models predictions are sensitive to the intrinsic axial ratio of the MGE models. This implies that for nearly face-on inclinations, where the intrinsic axial ratio of the models change rapidly, the inclination is formally constrained to a fraction of a degree. This formal accuracy is, however, compensated by a broader degeneracy in the mass deprojection, leading to a small *negative* bias in the inclination. In practice, for the four simulations we constructed (40 different projections in total), the errors never exceeded $5°$.

We confirm previous results that the M/L can be recovered within a few percent when the simulated galaxies are nearly axisymmetric, except for nearly face-on view ($i \lesssim 30°$), for which the M/L can be significantly overestimated. The global anisotropy β_z can be difficult to recover, especially at low inclination (near face-on) due to the inclination-anisotropy degeneracy. This degeneracy implies a significant uncertainty on β_z at low inclination, but a smaller error at high inclination. The global anisotropy is primarily influenced by the flattening (or the roundness) of the MGE parametrization of the projected luminosity. In the case of regular axisymmetric objects, the main issue is the intrinsic mathematical degeneracy of the luminosity deprojection at low inclination, which affects any axisymmetric deprojection method, including the adopted MGE one. This results in small deviations of the recovered global anisotropy from the value computed from the numerical simulations: β_z is well recovered.

When a bar is present, the mass deprojection becomes the main uncertainty in the models. The deprojected axisymmetric model will be naturally different from the true non-axisymmetric barred distribution and will change as a function of the observed PA. Consequently the predicted $V_{\rm rms}$ of the models, as well as the corresponding best fitting β_z will change as a function of the PA and can be quite different from the true axially-averaged value.

The mass-to-light ratio is less sensitive to the MGE parametrization than the global anisotropy, but it is biased due to the intrinsic dynamics of the system we want to model. We find that M/L is mainly influenced by the position of the bar and the size of the field of view. The error depends upon the position angle of the bar $PA_{\rm bar}$ and can be up to 15%. Including only regions far from the bar allows a reduction of the error, but cannot generally avoid it completely.

Our study provides an estimate of the M/L error that can affect the determination of dynamical M/L via axisymmetric models, and in particular using the JAM method. The large variety of possible shapes, sizes and orientations of bars in galaxies, each with specific dynamics, prevents us from quantifying the exact errors made for individual galaxies. One should also keep in mind that our study is done on simulations of relatively weak bars. Therefore, the error on the estimated M/L when modelling galaxies exhibiting stronger bars is expected to be larger. The objects studied here are still representative ATLAS[3D] fast rotators, this study therefore providing clear guidelines when applying axisymmetric modelling to such large samples.

REFERENCES

Binney, J. J., Davies, R. L., & Illingworth, G. D. 1990, Apj, 361, 78

Binney, J. 2005, MNRAS, 363, 937

Binney, J., & Tremaine, S. 1987, Princeton, NJ, Princeton University Press, 1987, 747 p.

Bournaud, F., et al. 2007, Science, 316, 1166

Cappellari, M. 2002, MNRAS, 333, 400

Cappellari, M., & Copin, Y. 2003, MNRAS, 342, 345

Cappellari, M., et al. 2006, MNRAS, 366, 1126

Cappellari, M., et al. 2007, MNRAS, 379, 418

Cappellari, M. 2008, MNRAS, 390, 71

Cappellari, M., et al. 2011a, MNRAS, 413, 813

Cappellari, M., Emsellem, E., Krajnović, D., et al. 2011b, MNRAS, 416, 1680

Cappellari, M., McDermid, R. M., Alatalo, K., et al. 2012, arXiv:1202.3308

Cretton, N., de Zeeuw, P. T., van der Marel, R. P., & Rix, H.-W. 1999, Apjs, 124, 383

Emsellem, E., Monnet, G., & Bacon, R. 1994a, AAp, 285, 723

Emsellem, E., Monnet, G., Bacon, R., & Nieto, J.-L. 1994b, AAp, 285, 739

Emsellem, E., et al. 2004, MNRAS, 352, 721

Emsellem, E., Cappellari, M., Krajnović, D., et al. 2011, MNRAS, 414, 888

Gebhardt, K., et al. 2003, Apj, 583, 92

Gerhard, O. 1996, Spiral Galaxies in the Near-IR, 138

Häfner, R., Evans, N. W., Dehnen, W., & Binney, J. 2000, MNRAS, 314, 433

Hernquist, L. 1990, ApJ, 356, 359

Jeans, J. H. 1922, MNRAS, 82, 122

Krajnović, D., Cappellari, M., Emsellem, E., McDermid, R. M., & de Zeeuw, P. T. 2005, MNRAS, 357, 1113

Krajnović, D., Emsellem, E., Cappellari, M., et al. 2011, MNRAS, 414, 2923

de Lorenzi, F., Debattista, V. P., Gerhard, O., & Sambhus, N. 2007, MNRAS, 376, 71

Michel-Dansac, L. & Wozniak, H., 2006, A&A, 452, 97

Monnet, G., Bacon, R., & Emsellem, E. 1992, AAp, 253, 366

Pfenniger, D. 1984, AAp, 134, 373

Poveda, A. 1958, Boletin de los Observatorios Tonantzintla y Tacubaya, 2, 3

Rybicki, G. B. 1987, Structure and Dynamics of Elliptical Galaxies, 127, 397

Schwarzschild, M. 1979, ApJ, 232, 236

Scott, N., et al. 2009, MNRAS, 398, 1835

Spitzer, L., Jr. 1969, Apjl, 158, L139

Thomas, J., Saglia, R. P., Bender, R., Thomas, D., Gebhardt, K., Magorrian, J., & Richstone, D. 2004, MNRAS, 353, 391

Thomas, J., Jesseit, R., Naab, T., Saglia, R. P., Burkert, A., & Bender, R. 2007, MNRAS, 381, 1672

Thomas, J., et al. 2009, MNRAS, 393, 641

Valluri, M., Merritt, D., & Emsellem, E. 2004, Apj, 602, 66

van den Bosch, R. C. E., van de Ven, G., Verolme, E. K., Cappellari, M., & de Zeeuw, P. T. 2008, MNRAS, 385, 647

van den Bosch, R. C. E., & van de Ven, G. 2009, MNRAS, 398, 1117

van der Marel, R. P., Binney, J., & Davies, R. L. 1990, MNRAS, 245, 582

van der Marel, R. P., Cretton, N., de Zeeuw, P. T., & Rix, H.-W. 1998, Aapj, 493, 613

Zhao, H. 1996, MNRAS, 283, 149

APPENDIX A: SIMULATIONS PROJECTED DENSITY

We present here the projected density maps for the simulations used in the present study at two different scales.

APPENDIX B: MGE DEPROJECTION

We illustrate with the following figure the intrinsic degeneracy present in the derojection process of inclined galaxies.

APPENDIX C: JAM RECOVERY SUMMARY

APPENDIX D: JAM FITTING
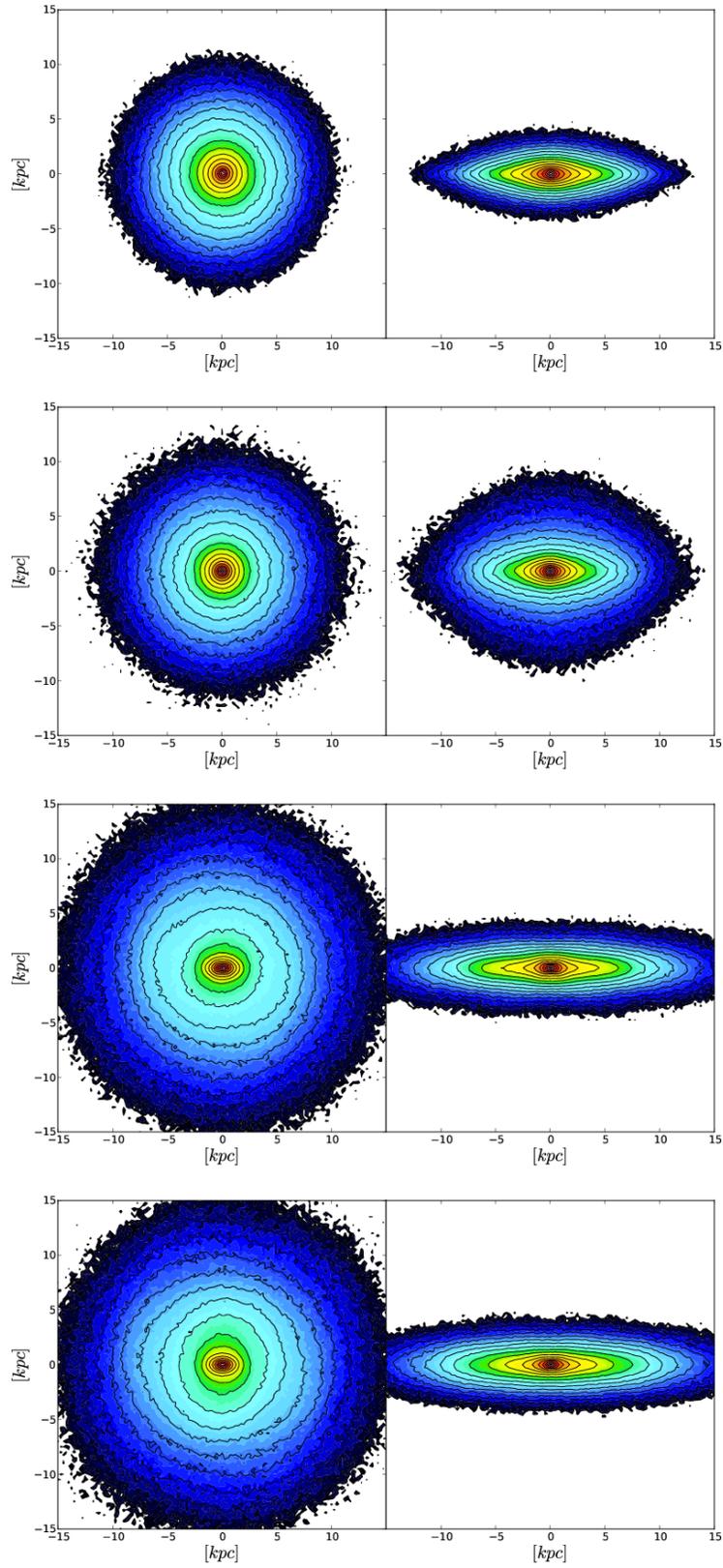
Figure A1. Face-on (left panels) and edge-on (right panels) projections of the final state of the four simulations. From top to bottom : $N4179axi$, $N4570axi$, $N4442bar$ and $N4754bar$.
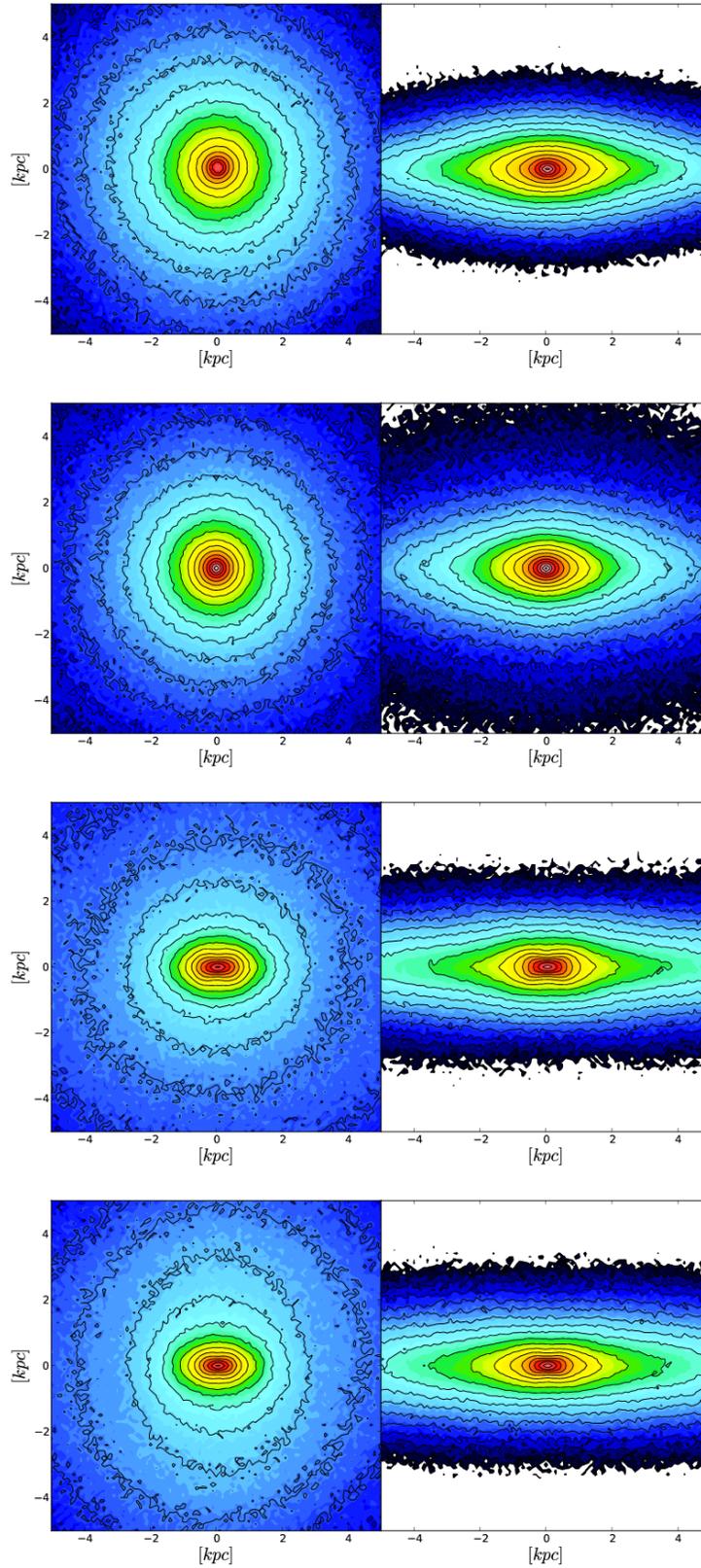
Figure A2. Same as Fig A1 with a field of view of 10*kpc* × 10*kpc*.
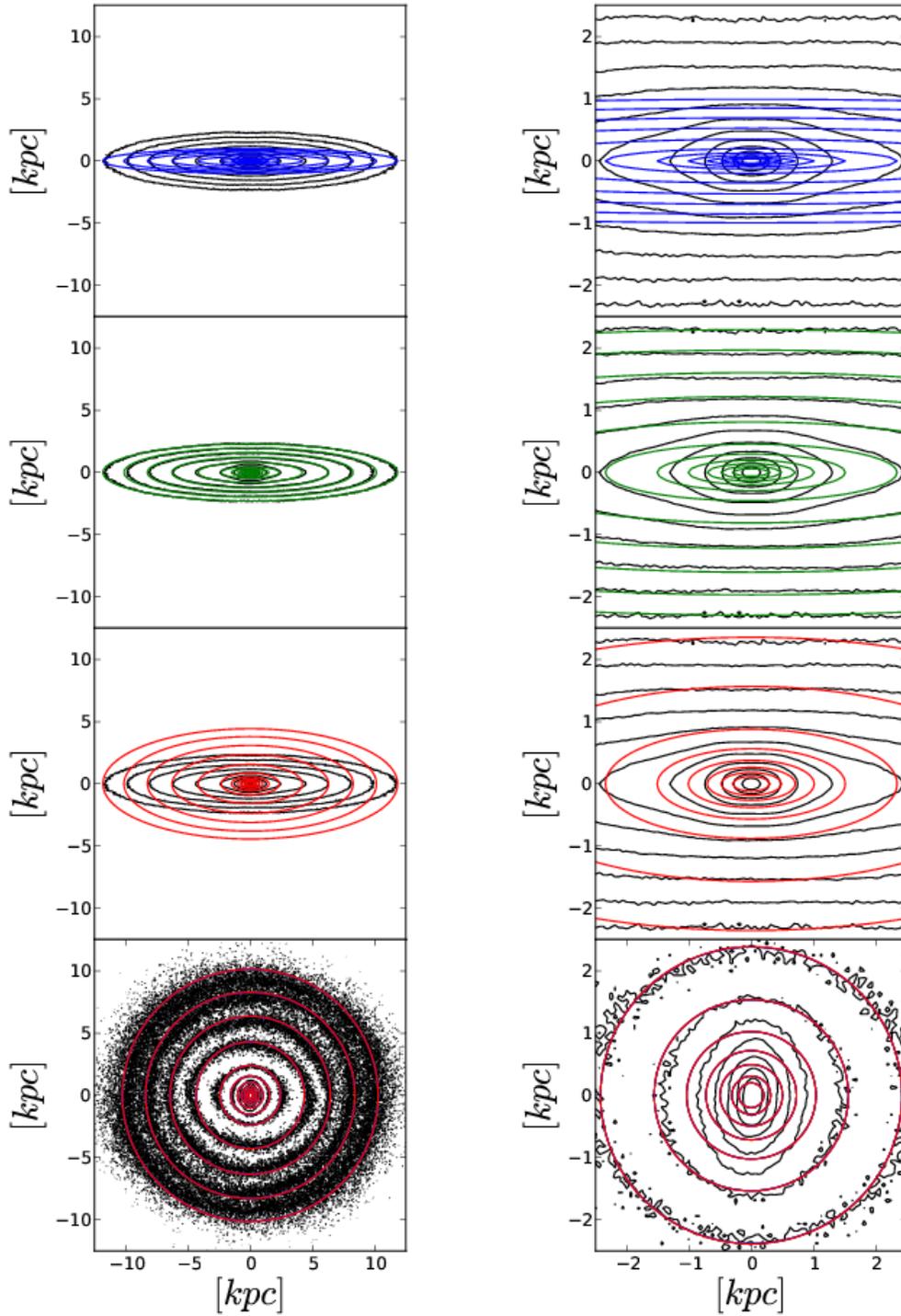
Figure B1. Degeneracy in the edge-on deprojected luminosity with a field of view pf $15kpc \times 15kpc$ (left column) and $5kpc \times 5kpc$ (right column). The first three rows represent the edge-on deprojection of MGE models with an apparent axis ratio $q' = 0.907$, $q' = 0.910$ and $q' = 0.920$ (from top to bottom respectively) when $i = 25°$, superposed to the edge-on averaged projected luminosity of $N4754bar$ (black contours). In the last row the projected luminosity with $i = 25°$ is ploted for all the three previous MGE models in addition to the luminosity contours of $N4754bar$ with $i = 25°$ and $PA_{bar} = 87°$. We see that in this latter case, even though the projected models are indistinguishable, the deprojected ones can be very different. This is a manifestation of the unavoidable intrinsic degeneracy in the mass deprojection of axisymmetric bodies at low inclination.

Model	i_{SIM}	$\mathrm{PA}_{\mathrm{bar}}$	i_{JAM}	β_z^{SIM}	β_z^{JAM}	M/L_{vir}	M/L_{JAM}	M/L Error in %
N4179axi	25	∅	23.8	0.106	0.4	6.29	6.87	9.22
	45	∅	43.1	0.106	0.2	6.29	6.36	1.11
	60	∅	59.4	0.106	0.05	6.29	6.30	0.16
	87	∅	84.9	0.106	0.1	6.29	6.26	0.48
N4570axi	25	∅	22.4	0.145	0.25	16.93	18.43	8.86
	45	∅	46.9	0.145	0.1	16.93	16.80	0.77
	60	∅	60.7	0.145	0.1	16.93	17.10	1.00
	87	∅	82.9	0.145	0.1	16.93	16.97	0.24
N4442bar	25	18	30.9	0.344	0.25	17.99	17.58	2.28
	25	45	27.3	0.344	0.55	17.99	21.82	21.29
	25	60	25.9	0.344	0.6	17.99	23.25	29.24
	25	87	24.3	0.344	0.35	17.99	22.51	25.13
	45	18	48.2	0.344	0.45	17.99	16.72	7.06
	45	45	45.6	0.344	0.1	17.99	17.67	1.78
	45	60	44.9	0.344	0.0	17.99	18.86	4.84
	45	87	44.3	0.344	0.0	17.99	19.93	10.78
	60	18	60.0	0.344	0.6	17.99	15.74	12.51
	60	45	59.3	0.344	0.2	17.99	17.63	2.00
	60	60	60.7	0.344	0.05	17.99	18.40	2.28
	60	87	60.6	0.344	0.0	17.99	19.16	6.50
	87	18	85.8	0.344	0.25	17.99	17.62	2.06
	87	45	84.7	0.344	0.25	17.99	17.94	0.28
	87	60	84.6	0.344	0.2	17.99	18.04	0.28
	87	87	85.1	0.344	0.1	17.99	18.21	1.22
N4754bar	25	18	30.1	0.343	0.0	11.04	9.82	11.05
	25	45	27.7	0.343	0.3	11.04	10.70	3.08
	25	60	25.4	0.343	0.3	11.04	12.18	10.33
	25	87	22.5	0.343	0.15	11.04	13.73	24.37
	45	18	51.4	0.343	0.0	11.04	10.42	5.62
	45	45	44.9	0.343	0.6	11.04	11.20	1.45
	45	60	44.6	0.343	0.6	11.04	11.98	8.51
	45	87	43.9	0.343	0.6	11.04	12.78	15.76
	60	18	65.8	0.343	0.0	11.04	10.50	4.89
	60	45	59.4	0.343	0.6	11.04	11.28	2.17
	60	60	59.6	0.343	0.05	11.04	11.68	5.80
	60	87	59.4	0.343	0.0	11.04	12.16	10.14
	87	18	86.2	0.343	0.2	11.04	11.05	0.09
	87	45	85.5	0.343	0.2	11.04	11.42	3.44
	87	60	84.7	0.343	0.2	11.04	11.64	5.43
	87	87	85.1	0.343	0.1	11.04	11.81	6.97

Table C1. Table summarizing the values of i, $\mathrm{PA}_{\mathrm{bar}}$, β_z and M/L of our mock observations and the values recovered by the JAM modelling method.
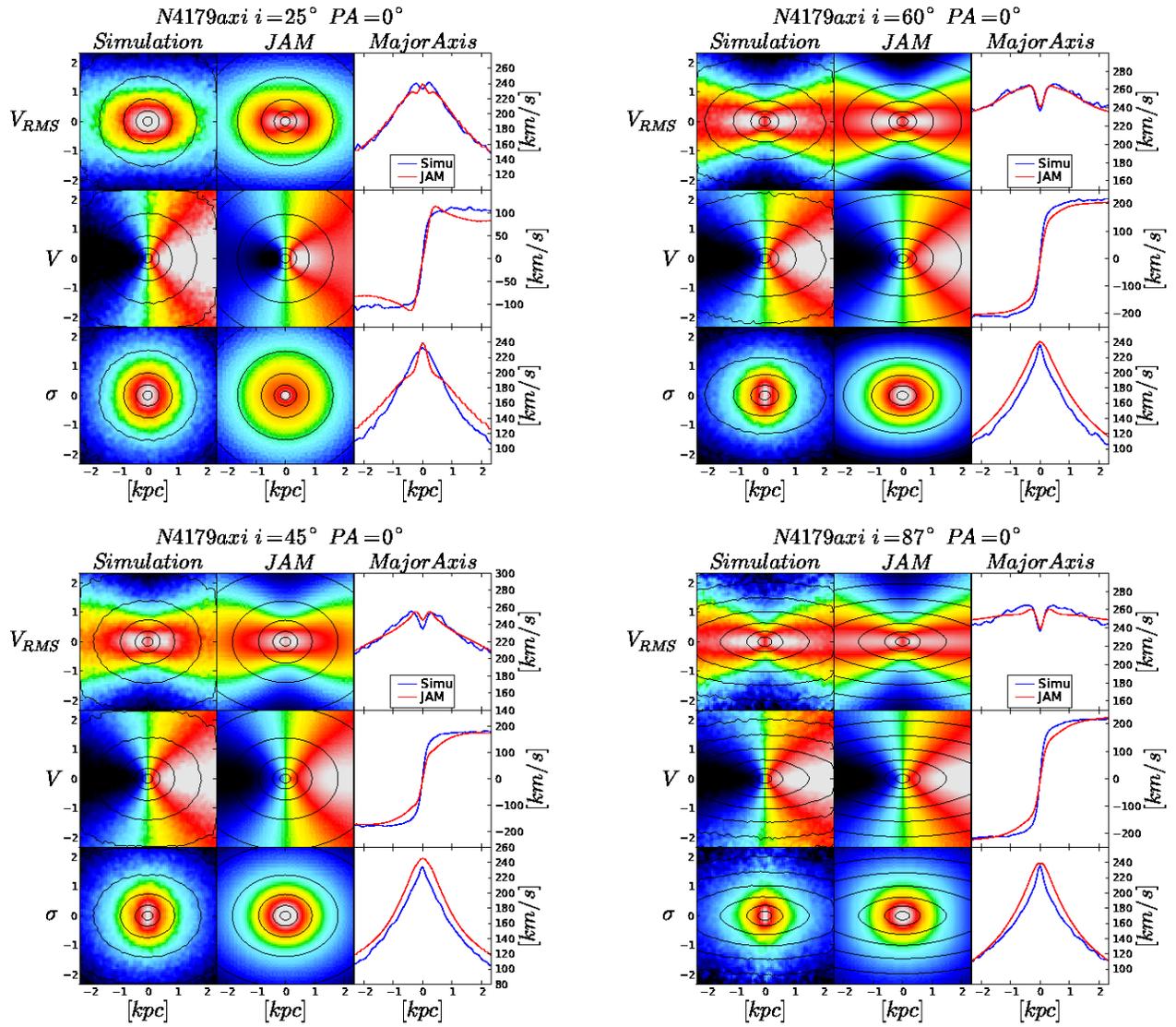
Figure D1. Comparison between the simulations projected velocity maps and the best JAM fitting for $N4179axi$ for the four angles of projection.
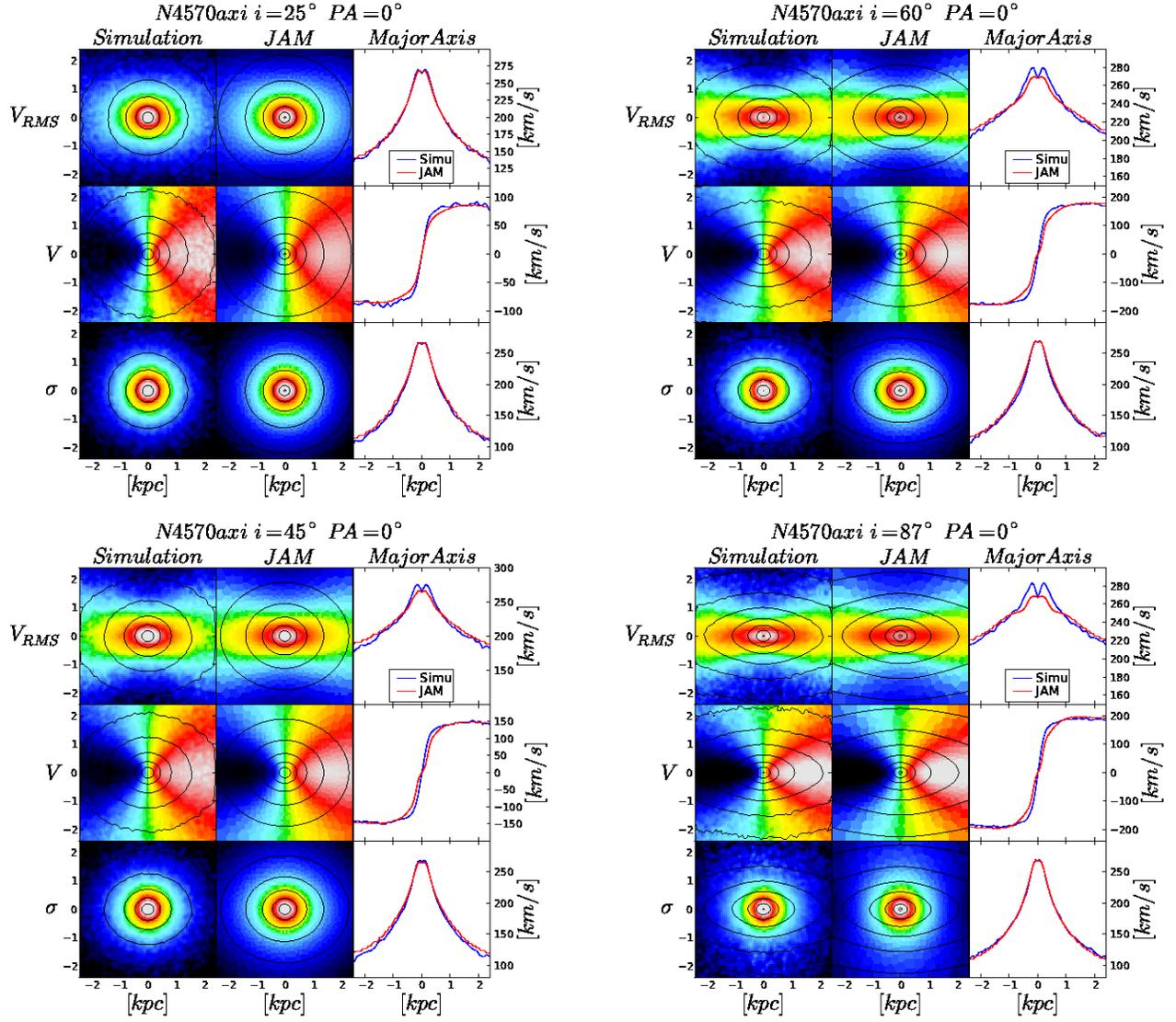
Figure D2. Comparison between the simulations projected velocity maps and the best JAM fitting for $N4570axi$ for the four angles of projection.
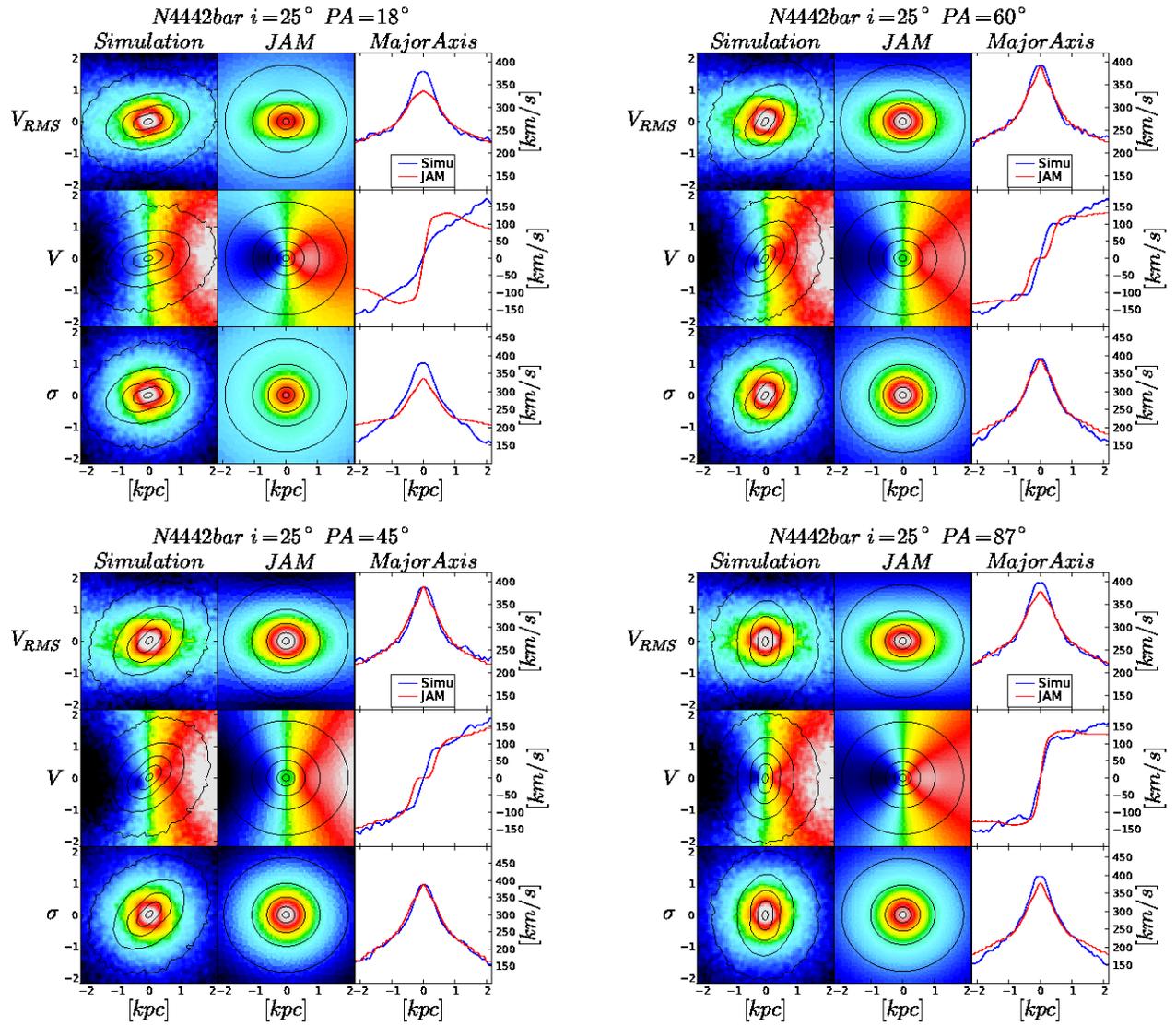
Figure D3. Comparison between the simulations projected velocity maps and the best JAM fitting for $N4442bar$ for $i = 25°$ and the four PA$_{\text{bar}}$.
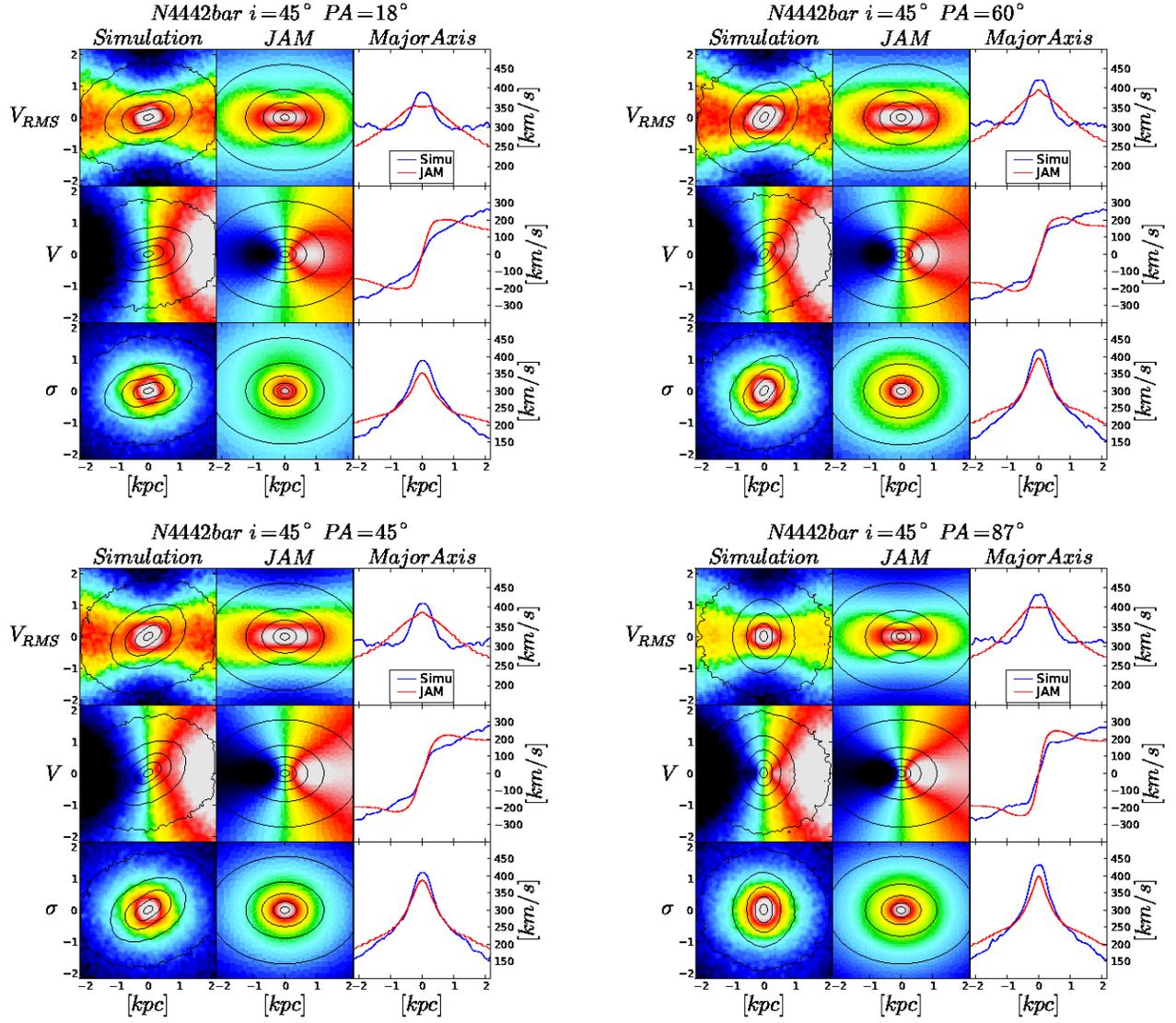
Figure D4. Comparison between the simulations projected velocity maps and the best JAM fitting for $N4442bar$ for $i = 45°$ and the four PA$_{\text{bar}}$.
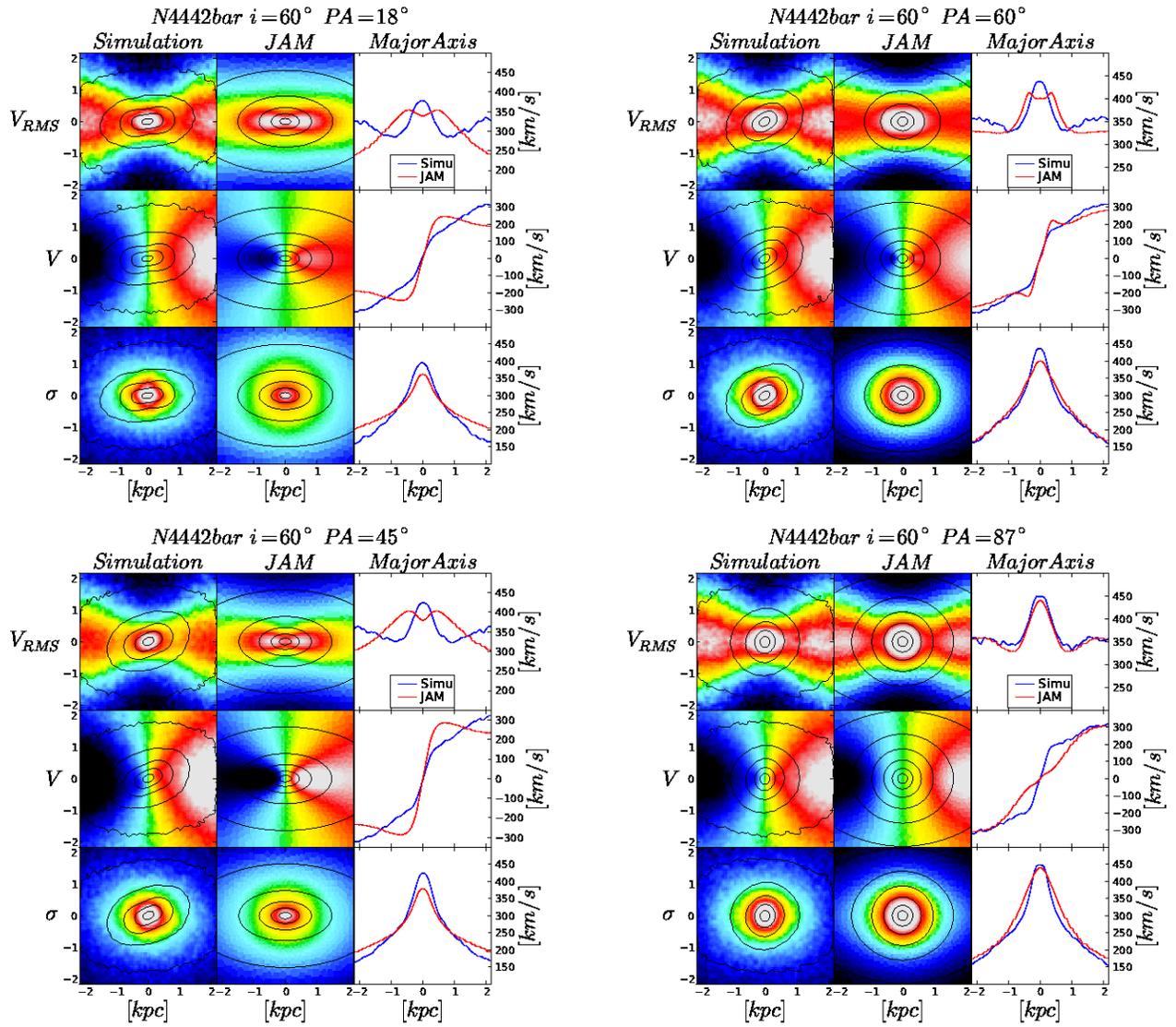
Figure D5. Comparison between the simulations projected velocity maps and the best JAM fitting for $N4442bar$ for $i = 60°$ and the four PA_{bar}.
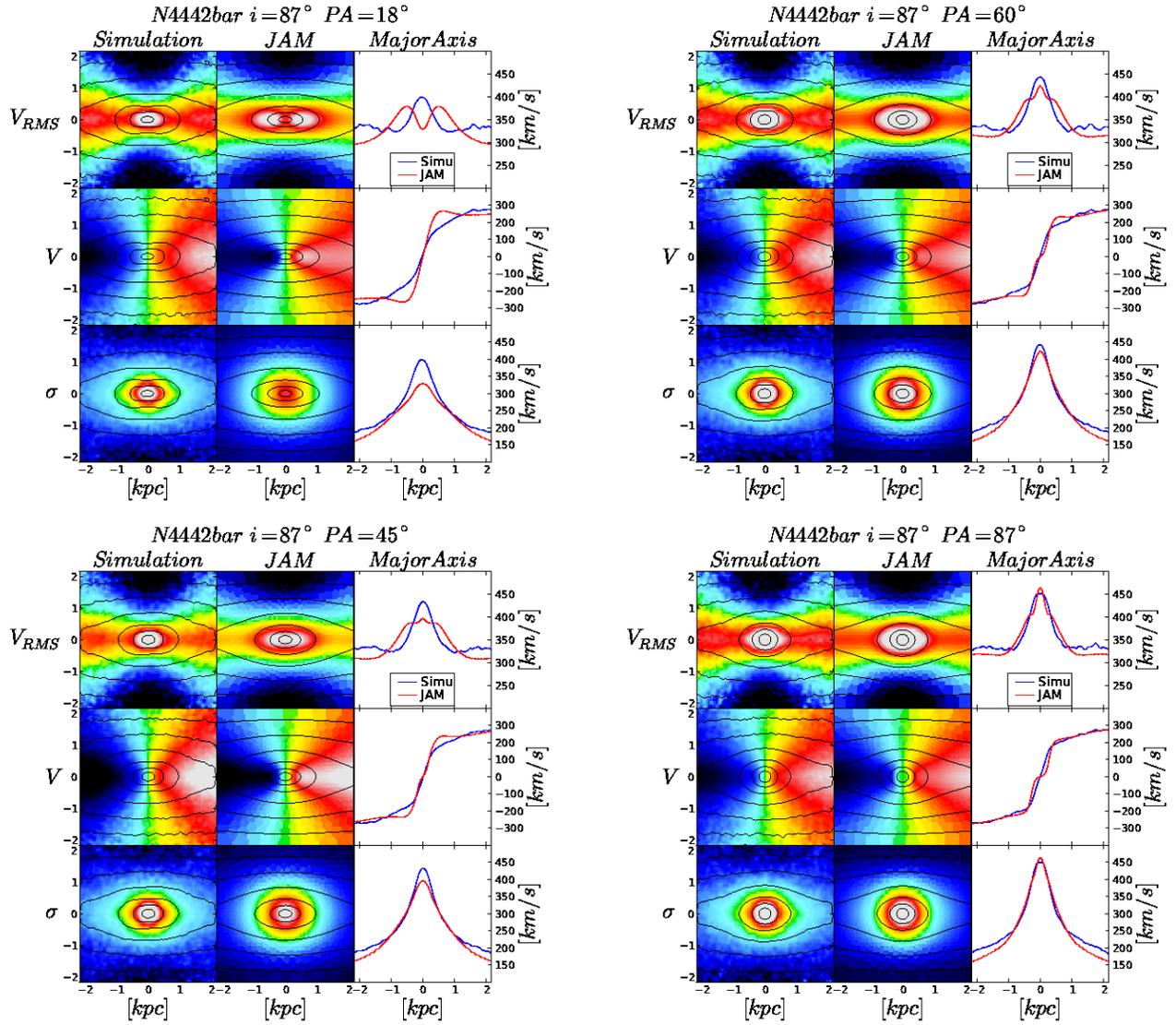
Figure D6. Comparison between the simulations projected velocity maps and the best JAM fitting for $N4442bar$ for $i = 87°$ and the four PA$_{\mathrm{bar}}$.
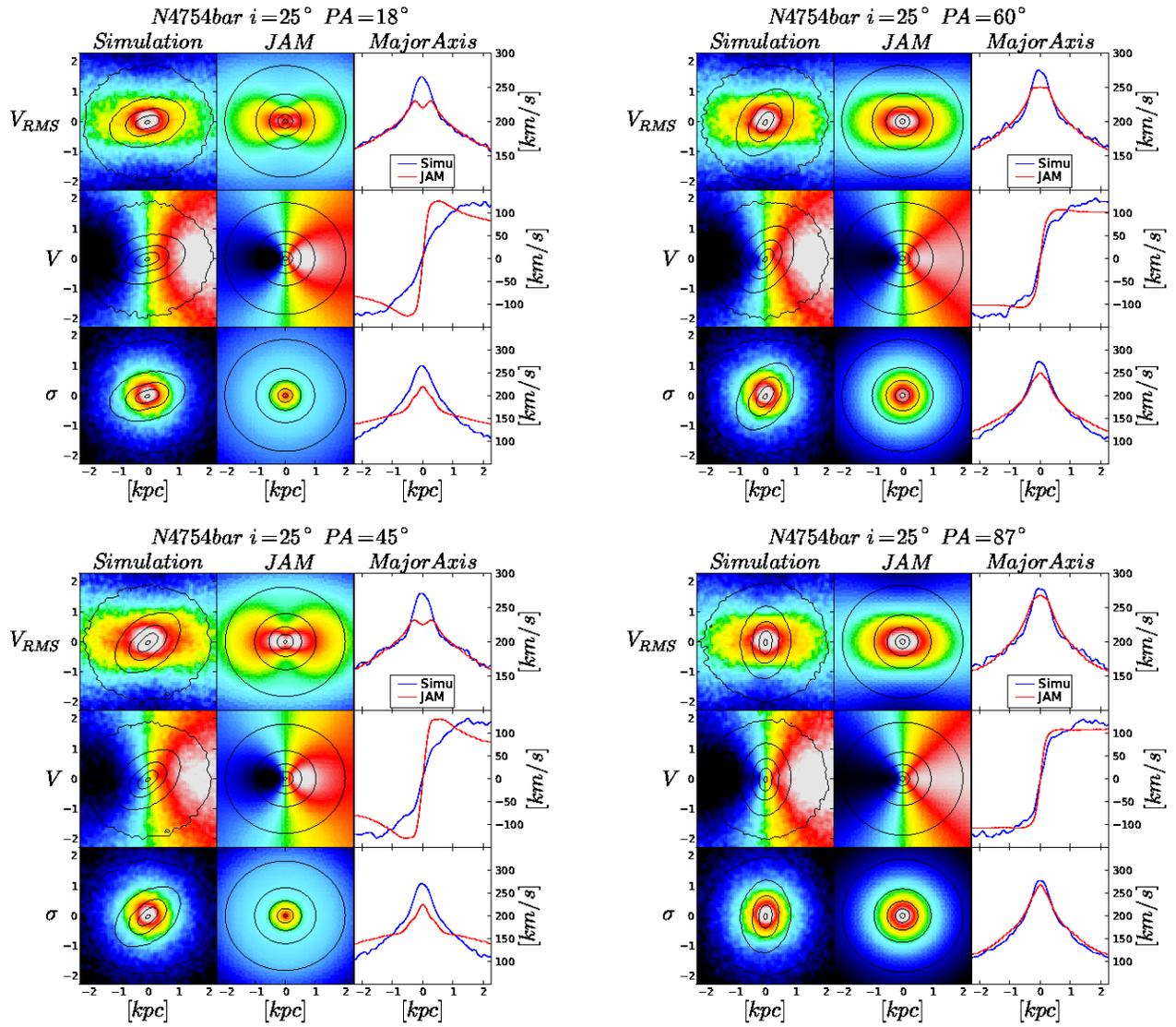
Figure D7. Comparison between the simulations projected velocity maps and the best JAM fitting for $N4754bar$ for $i = 25°$ and the four PA$_{bar}$.
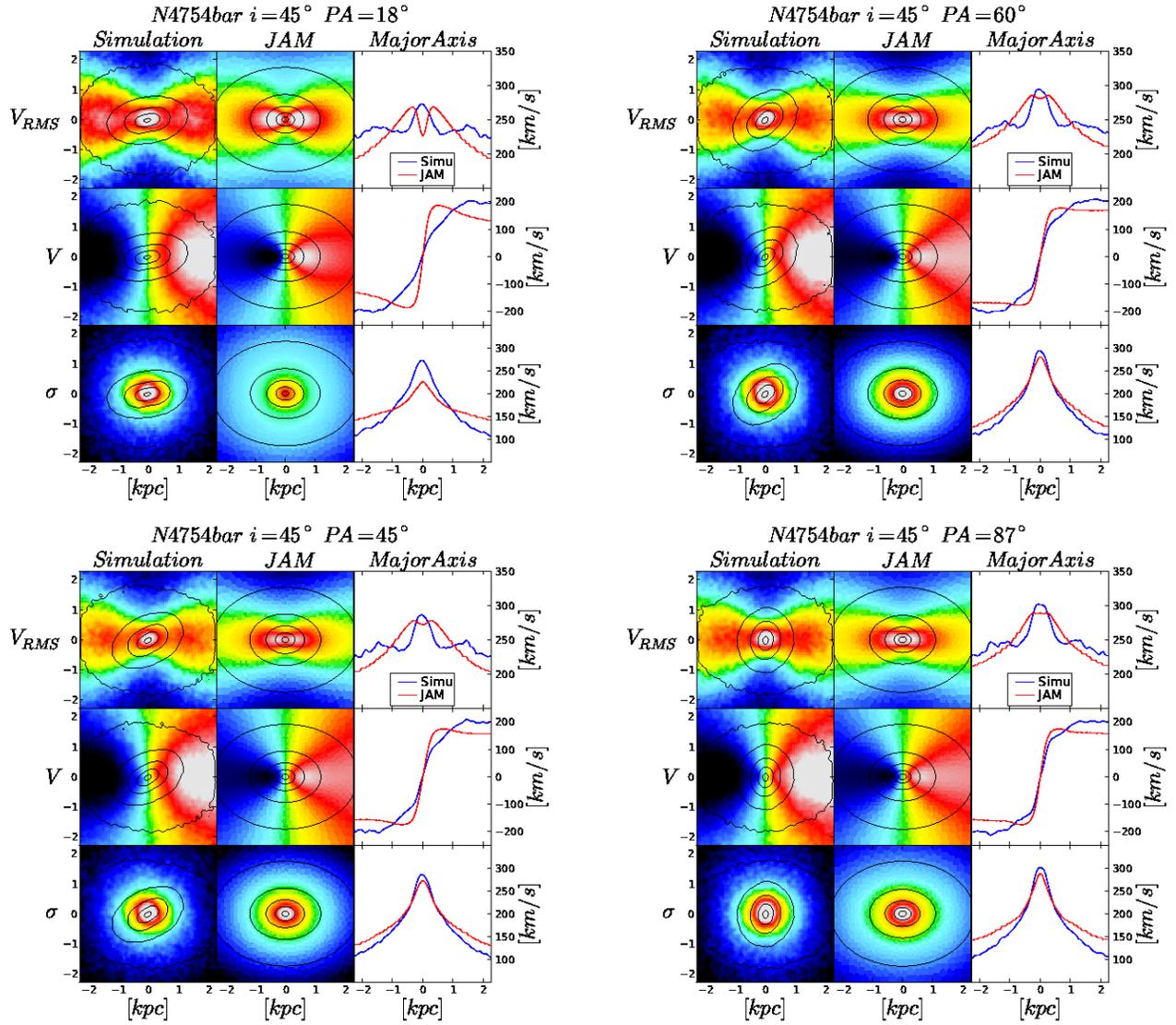
Figure D8. Comparison between the simulations projected velocity maps and the best JAM fitting for $N4754bar$ for $i = 45°$ and the four PA$_{\rm bar}$.
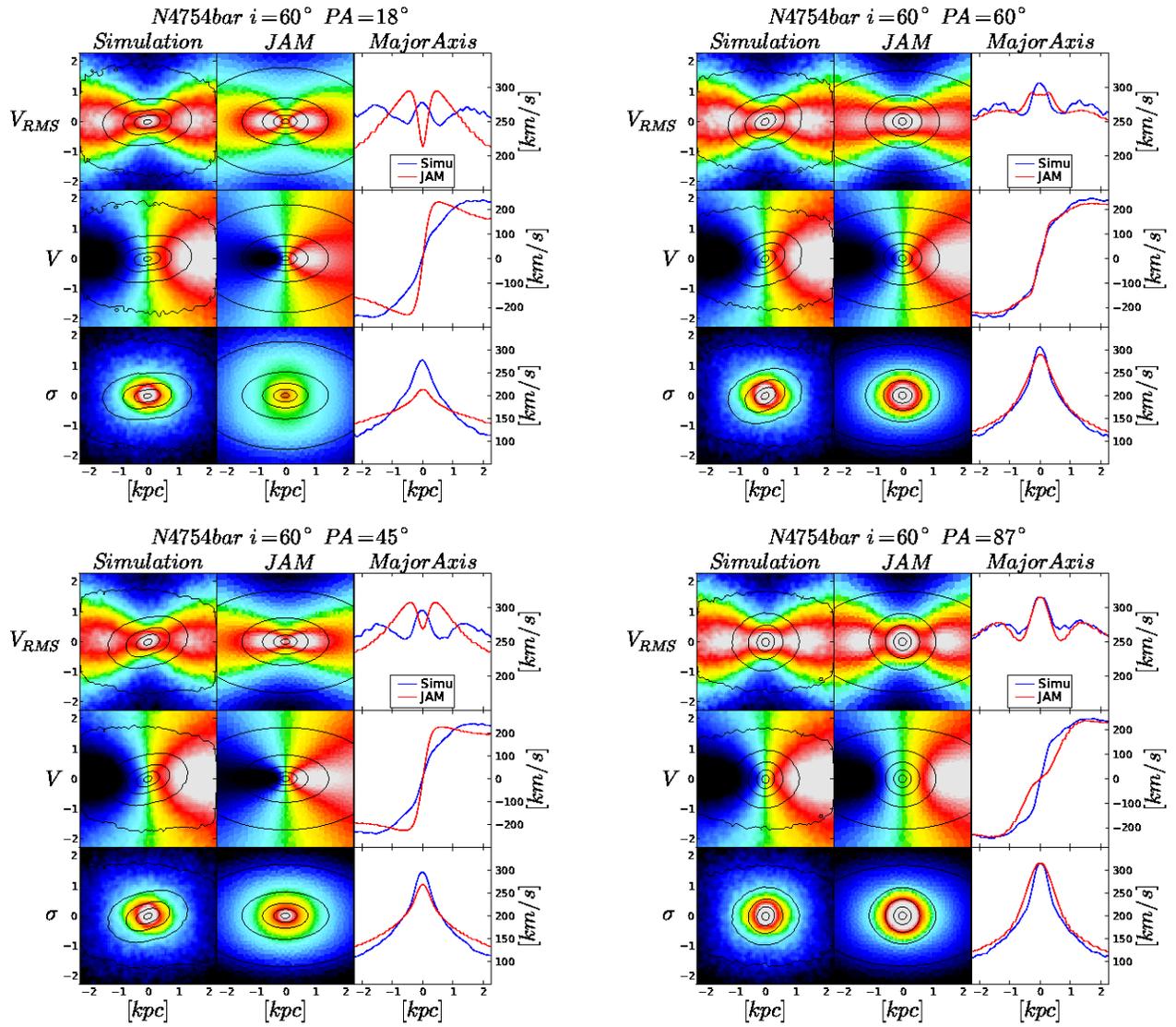
Figure D9. Comparison between the simulations projected velocity maps and the best JAM fitting for $N4754bar$ for $i = 60°$ and the four PA_{bar}.
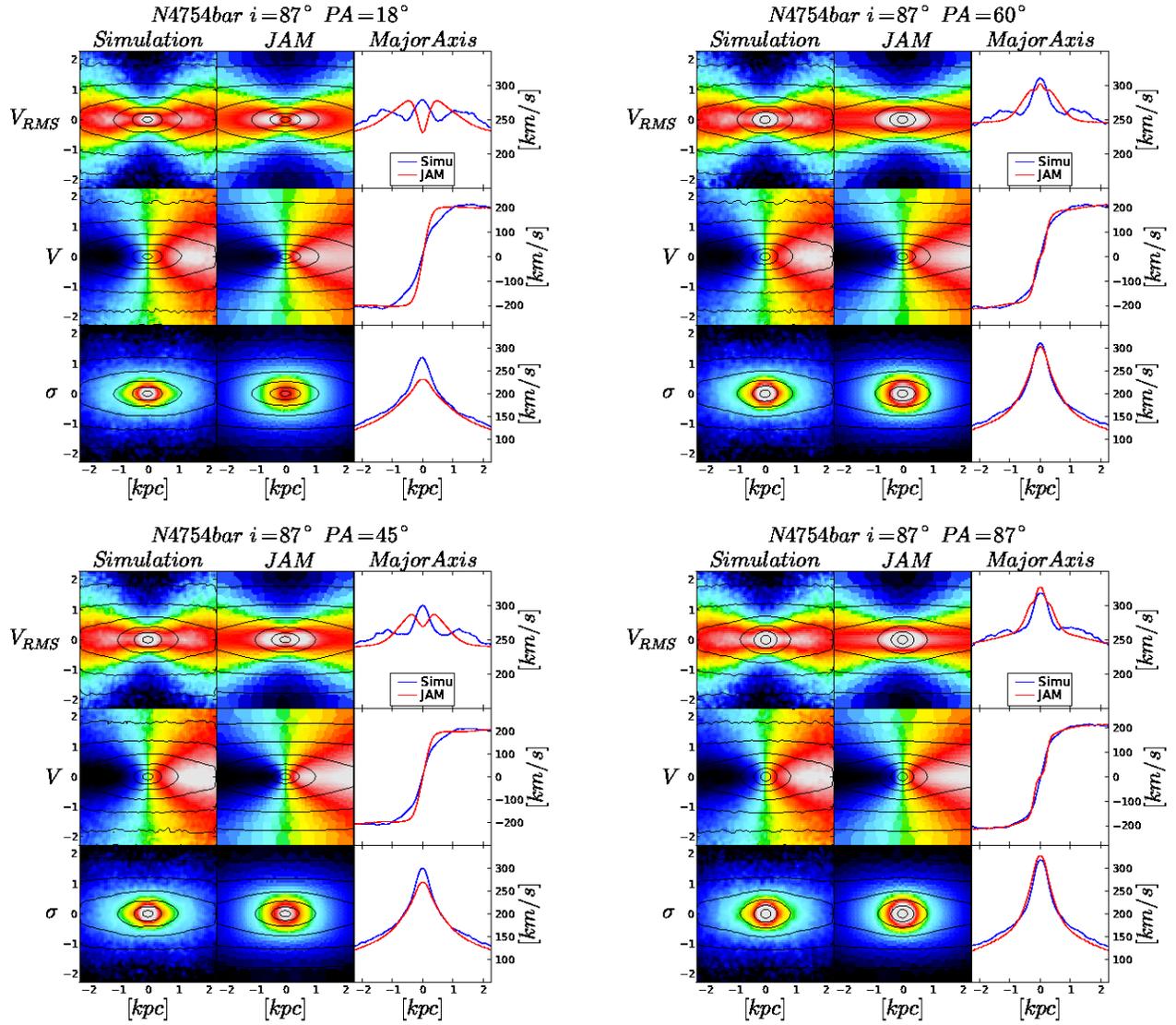
Figure D10. Comparison between the simulations projected velocity maps and the best JAM fitting for $N4754bar$ for $i = 87°$ and the four PA_{bar}.